The baryonic specific angular momentum of disc galaxies

Pavel E. Mancera Piña, Lorenzo Posti, Filippo Fraternali, Elizabeth A.K. Adams, Tom Oosterloo

Pavel E. Mancera Piña, Lorenzo Posti, Filippo Fraternali, Elizabeth A.K. Adams, Tom Oosterloo. The baryonic specific angular momentum of disc galaxies. Astronomy & Astrophysics - A&A, 2021, 647, pp.A76. ⟨10.1051/0004-6361/202039340⟩. ⟨hal-02966270⟩

HAL Id: hal-02966270
https://hal.science/hal-02966270v1

Submitted on 10 Jun 2022

A&A 647, A76 (2021)
https://doi.org/10.1051/0004-6361/202039340
© ESO 2021

Astronomy & Astrophysics

The baryonic specific angular momentum of disc galaxies★

Pavel E. Mancera Piña[1,2], Lorenzo Posti[3], Filippo Fraternali[1], Elizabeth A. K. Adams[2,1], and Tom Oosterloo[2,1]

[1] Kapteyn Astronomical Institute, University of Groningen, Landleven 12, 9747 AD Groningen, The Netherlands
e-mail: `pavel@astro.rug.nl`
[2] ASTRON, Netherlands Institute for Radio Astronomy, Postbus 2, 7900 AA Dwingeloo, The Netherlands
[3] Observatoire Astronomique de Strasbourg, Université de Strasbourg, 11 Rue de l'Université, 67000 Strasbourg, France

Received 4 September 2020 / Accepted 2 January 2021

ABSTRACT

Aims. Specific angular momentum (the angular momentum per unit mass, $j = J/M$) is one of the key parameters that control the evolution of galaxies, and it is closely related with the coupling between dark and visible matter. In this work, we aim to derive the baryonic (stars plus atomic gas) specific angular momentum of disc galaxies and study its relation with the dark matter specific angular momentum.

Methods. Using a combination of high-quality H I rotation curves, H I surface densities, and near-infrared surface brightness profiles, we homogeneously measure the stellar (j_*) and gas ($j_{\rm gas}$) specific angular momenta for a large sample of nearby disc galaxies. This allows us to determine the baryonic specific angular momentum ($j_{\rm bar}$) with high accuracy and across a very wide range of masses.

Results. We confirm that the j_*–M_* relation is an unbroken power-law from $7 \lesssim \log(M_*/M_\odot) \lesssim 11.5$, with a slope 0.54 ± 0.02, setting a stronger constraint at dwarf galaxy scales than previous determinations. Concerning the gas component, we find that the $j_{\rm gas}$–$M_{\rm gas}$ relation is also an unbroken power-law from $6 \lesssim \log(M_{\rm gas}/M_\odot) \lesssim 11$, with a steeper slope of 1.02 ± 0.04. Regarding the baryonic relation, our data support a correlation characterized by a single power-law with a slope 0.60 ± 0.02. Our analysis shows that our most massive spirals and smallest dwarfs lie along the same $j_{\rm bar}$–$M_{\rm bar}$ sequence. While the relations are tight and unbroken, we find internal correlations inside them: At fixed M_*, galaxies with larger j_* have larger disc scale lengths, and at fixed $M_{\rm bar}$, gas-poor galaxies have lower $j_{\rm bar}$ than expected. We estimate the retained fraction of baryonic specific angular momentum, $f_{j,\rm bar}$, finding it constant across our entire mass range with a value of ~0.6, indicating that the baryonic specific angular momentum of present-day disc galaxies is comparable to the initial specific angular momentum of their dark matter haloes. In general, these results set important constraints for hydrodynamical simulations and semi-analytical models that aim to reproduce galaxies with realistic specific angular momenta.

Key words. galaxies: kinematics and dynamics – galaxies: formation – galaxies: fundamental parameters – galaxies: evolution – galaxies: dwarf – galaxies: spiral

1. Introduction

Understanding the relation between the observed properties of galaxies and those expected from their parent dark matter haloes, as well as the physical processes that regulate such properties, is one of the major goals of present-day astrophysics.

Angular momentum, in addition to the total mass, arguably governs most stages of galaxy formation and evolution (e.g, Fall & Efstathiou 1980; Dalcanton et al. 1997; Mo et al. 1998). From its origin in a cold dark matter (CDM) universe via primordial tidal torques (Peebles 1969) to its repercussions on the morphology of present-day galaxies (e.g., Romanowsky & Fall 2012; Cortese et al. 2016; Lagos et al. 2018; Sweet et al. 2020; Kulier et al. 2020), angular momentum, or specific angular momentum if weighted by the total mass, plays a crucial role in shaping galaxies at all redshifts (e.g., Stevens et al. 2016; Posti et al. 2018a; Marasco et al. 2019; Sweet et al. 2019; Marshall et al. 2019). Yet, the exact interplay between the angular momentum of dark mater haloes and that of the baryons is not completely understood.

The 'retained fraction of angular momentum'– the ratio between the specific angular momentum of the baryons ($j_{\rm bar}$) and that of the parent dark matter halo ($j_{\rm h}$)– is one of the parameters of paramount importance in this context. Still, its behaviour as a function of galaxy mass or redshift (e.g., Romanowsky & Fall 2012; Posti et al. 2018a) has not yet been fully established on an observational basis.

Galaxy scaling relations can be reasonably well reproduced if this global fraction ($f_{j,\rm bar} = j_{\rm bar}/j_{\rm h}$) is close to unity (e.g., Dalcanton et al. 1997; Mo et al. 1998; Navarro & Steinmetz 2000); otherwise, scaling laws like the Tully–Fisher relation would be in strong disagreement with observations. In general, if $f_{j,\rm bar}$ is too low, then the baryons do not have enough angular momentum to reproduce the size distribution observed in present-day galaxies, giving rise to the so-called angular momentum catastrophe (see for instance Steinmetz & Navarro 1999; D'Onghia et al. 2006; Dutton & van den Bosch 2012; Somerville et al. 2018; Cimatti et al. 2019). These problems are mitigated by including the effects of stellar and active galactic nucleus feedback, which prevent the ratio $f_{j,\rm bar}$ from being too small (e.g., Governato et al. 2007; Dutton & van den Bosch 2012). These and other phenomena, such as galactic fountains or angular momentum transfer between baryons and dark matter, also participate in shaping the detailed local baryonic angular momentum distribution within galaxies (e.g., van den Bosch et al. 2001; Cimatti et al. 2019; Sweet et al. 2020).

★ Full Table 1 is only available at the CDS via anonymous ftp to `cdsarc.u-strasbg.fr` (`130.79.128.5`) or via `http://cdsarc.u-strasbg.fr/viz-bin/cat/J/A+A/647/A76`

In a pioneering work, Fall (1983) first determined the shape of the stellar specific angular momentum–mass relation (the j_*–M_* relation); because of this, the j–M laws are sometimes called Fall relations. The results from Fall (1983) were later confirmed in the literature with more and better data (e.g., Romanowsky & Fall 2012; Fall & Romanowsky 2018). Particularly, Posti et al. (2018a, hereafter P18) recently studied the j_*–M_* relation relation with a large sample of disc galaxies with extended and high-quality rotation curves, also taking subtle effects, such as the difference in the rotation of gas and stars, into account.

The general picture of these studies is that disc galaxies define a tight sequence in the j_*–M_* plane, following an unbroken power-law with a slope around 0.5–0.6. Early-type galaxies follow a similar trend, but with a lower intercept such that, at a given M_*, they have about five times less j_* than late-type galaxies (Fall 1983; Romanowsky & Fall 2012). The fact that the slope of the relation is 0.5–0.6 is remarkable as this value is very close to the slope of the relation of dark matter haloes, $j_\mathrm{h} \propto M_\mathrm{h}^{2/3}$ (e.g., Fall 1983; Romanowsky & Fall 2012; Obreschkow & Glazebrook 2014; P18, and references therein).

While these studies have built a relatively coherent picture of the stellar component, the gas (j_gas–M_gas) and baryonic (j_bar–M_bar) relations remain somewhat less well explored, although studies performed in recent years have started to delve into this (Obreschkow & Glazebrook 2014; Butler et al. 2017; Chowdhury & Chengalur 2017; Elson 2017; Kurapati et al. 2018; Lutz et al. 2018; Murugeshan et al. 2020). In fact, different authors have reported different results regarding the nature of the j_bar–M_bar relation, such as whether or not the slope of the correlations in the j_bar–M_bar and j_*–M_* planes are the same, if dwarf galaxies follow a different sequence than higher-mass spirals, or whether or not the relations have a break at a characteristic mass.

This work focuses on homogeneously deriving the stellar, gas, and baryonic specific angular momenta of a large sample of disc galaxies with the best rotation curves and photometry data available. This manuscript is organized as follows. In Sect. 2, we describe the sample of galaxies used in this work. Section 3 contains our methods for deriving the specific angular momentum–mass relation for each component (stars, gas, baryons), and Sect. 4 presents our main results. In Sect. 5 we discuss these results, including an empirical estimation of the retained fraction of specific angular momentum, and we summarize our findings and conclude in Sect. 6.

2. Building the sample

To compute the baryonic specific angular momentum, we needed to determine the contribution of the stellar (j_*) and gas (j_gas) components, as described in detail in Sect. 3. To obtain the stellar and gas specific angular momenta, stellar and gas surface density profiles are necessary, together with extended rotation curves. In their study of j_*, P18 used the galaxies in the *Spitzer* Photometry and Accurate Rotation Curves database (SPARC, Lelli et al. 2016a). Unfortunately, radial H I surface density profiles are not available in SPARC. Because of this, we built a compilation of galaxies with high-quality H I and stellar surface density profiles and extended rotation curves from different samples in the literature. In the rest of this section we describe these samples.

We started by considering the SPARC galaxies (rotation curves and stellar surface density profiles) for which H I surface density profiles are available from the original sources or authors (Begeman 1987; Sanders 1996; Sanders & Verheijen 1998; Fraternali et al. 2002, 2011; Swaters et al. 2002; Begum & Chengalur 2004; Battaglia et al. 2006; Boomsma 2007; de Blok et al. 2008; Verheijen & Sancisi 2001; Noordermeer 2006; Swaters et al. 2009). If needed, distance-dependent quantities were re-scaled to the distance given in SPARC.

We complemented these galaxies with the sample of disc galaxies compiled and analysed by Ponomareva et al. (2016). We only slightly modified the data provided by those authors: For a few galaxies we exclude the outermost $\lesssim$10% of the rotation curve, where it is not clear how well traced the emission of the galaxy is (see for instance NGC 224, NGC 2541, or NGC 3351 in their appendix). The radial coverage in these few galaxies is, however, still sufficiently extended, and the removal of those few points has no significant effect in the computation of j. Similarly to SPARC, the sample from Ponomareva et al. (2016) has 3.6 μm photometry (Ponomareva et al. 2017), which is needed to compute j_*, as we show in Sect. 3.

To populate the low-mass regime, which is not well sampled in SPARC, we took advantage of the recent and detailed analysis of dwarf galaxies from the Local Irregulars That Trace Luminosity Extremes, The H I Nearby Galaxy Survey (LITTLE THINGS, Hunter et al. 2012) by Iorio et al. (2017). These galaxies have 3.6 μm photometry from Zhang et al. (2012), except for DDO 47, which was therefore excluded from our sample.

Furthermore, we considered a set of dwarf galaxies from the Local Volume H I Survey (LVHIS, Koribalski et al. 2018), for which we derived accurate kinematic models using the software $^{\mathrm{3D}}$BAROLO (Di Teodoro & Fraternali 2015) in the same way as done in Iorio et al. (2017). We provide further details on this modelling in Appendix A. These galaxies have near-infrared photometry (H-band at 1.65 μm) available in the literature (Kirby et al. 2008; Young et al. 2014).

Finally, we considered a few dwarf galaxies from the Very Large Array-ACS Nearby Galaxy Survey Treasury (VLA-ANGST, Ott et al. 2012) and the Westerbork observations of neutral Hydrogen in Irregular and SPiral galaxies (WHISP, van der Hulst et al. 2001) projects, for which we also obtained kinematic models using $^{\mathrm{3D}}$BAROLO (see Appendix A). These dwarfs have publicly available 3.6 μm surface brightness profiles from Bouquin et al. (2018), except for UGC 10564 and UGC 12060, for which we built the 3.6 μm surface brightness profiles (see Marasco et al. 2019) from the data in the *Spitzer* Heritage Archive.

Stellar and gas masses were computed in the same way as in P18, by integrating the infrared and gas surface density profiles out to the last measured radius: $M_k = 2\pi \int_0^{R_\mathrm{max}} R' \Sigma_k(R') \mathrm{d}R'$. The near-infrared mass-to-light ratio Υ used to calculate M_* varies slightly depending on the available data. For galaxies in the SPARC database, that have available surface brightness profile decomposition, we assumed the same mass-to-light ratio as P18: $\Upsilon_\mathrm{d}^{3.6} = 0.5$ and $\Upsilon_\mathrm{b}^{3.6} = 0.7$ for the disc and bulge, respectively. For the rest of the galaxies with 3.6 μm data, which are disc-dominated, we adopted $\Upsilon_\mathrm{d}^{3.6} = 0.5$. For the LVHIS dwarfs, which have H-band photometry, we adopted $\Upsilon_\mathrm{d}^{H} = 1$ (see more details in Kirby et al. 2008; Young et al. 2014). For the mass gas, all the H I surface densities (Σ_HI) in the different samples were homogenized to include a helium correction such that $\Sigma_\mathrm{gas} = 1.33 \Sigma_\mathrm{HI}$.

After taking out the galaxies that overlap between the different subsamples, we ended up with 90 from SPARC and the above references, 30 from the Ponomareva et al. (2016) sample, 16 from LITTLE THINGS, 14 from LVHIS, four from VLA-ANGST, and three from WHISP. This gave us a total of 157 galaxies, making this the largest sample for which detailed

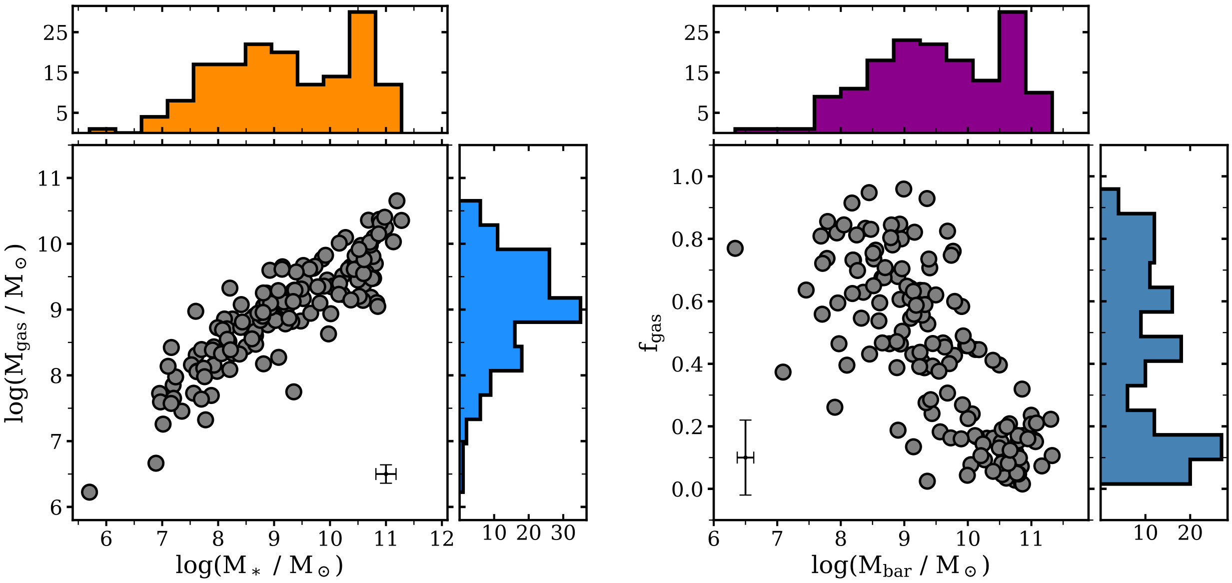

Fig. 1. M_*–$M_{\rm gas}$ (*left*) and $M_{\rm bar}$–$f_{\rm gas}$ (*right*) relation for our sample of galaxies. Typical errorbars are shown in black. The panels at the *top* and *right* of each relation show the histograms of the M_*, $M_{\rm gas}$, $M_{\rm bar}$, and $f_{\rm gas}$ distributions.

derivations of the three j–M laws have been performed to date. This sample, like the SPARC database, is not volume-limited, but it is representative of nearby regularly rotating galaxies. It is also worth mentioning that the high-quality rotation curves for all the galaxies were derived from the same type of data (HI interferometric observations) using consistent techniques (tilted ring models, e.g., Di Teodoro & Fraternali 2015), so we do not expect any systematic bias between the different subsamples. Our final sample of galaxies spans a mass range of $6 \lesssim \log(M_*/M_\odot) \lesssim 11.5$ and $6 \lesssim \log(M_{\rm gas}/M_\odot) \lesssim 10.5$, with a wide spread of gas fractions ($f_{\rm gas} = M_{\rm gas}/M_{\rm bar}$). Figure 1 shows the M_*–$M_{\rm gas}$ and $M_{\rm bar}$–$f_{\rm gas}$ relations for our sample, together with their 1D distributions. The rotation curves and surface density profiles are extended, with a median ratio between the maximum extent of the rotation curve $R_{\rm out}$ and the optical disc scale length $R_{\rm d}$ of ∼6, and with a 84th percentile of the $R_{\rm out}/R_{\rm d}$ distribution of ∼10.

3. Determining the specific angular momentum

3.1. Measuring $j_{\rm gas}$ and j_*

In a rotating galaxy disc, the specific angular momentum inside a radius R with rotation velocity V, for a given component k (stars or gas), is given by the expression:

$$j_k(<R) = \frac{2\pi \int_0^R R'^2\, \Sigma_k(R')\, V_k(R')\, {\rm d}R'}{2\pi \int_0^R R'\, \Sigma_k(R')\, {\rm d}R'}. \tag{1}$$

For the gas, the velocity profile that goes into Eq. (1) is simply $V_{\rm rot}$, the rotation velocity traced by the H I rotation curve. For the stars, co-rotation with the gas is often assumed ($V_* = V_{\rm rot}$). In such a case, given that $\Sigma_{\rm bar} = \Sigma_{\rm gas} + \Sigma_*$, $j_{\rm bar}$ is computed by taking $\Sigma_k = \Sigma_{\rm bar}$ and $V_k = V_{\rm rot}$ in Eq. (1).

Nonetheless, a more careful determination of j_* and $j_{\rm bar}$ should not assume $V_* = V_{\rm rot}$ (e.g., P18). This is because in practice stars usually rotate more slowly than the cold gas as they have a larger velocity dispersion. Even if this effect is not expected to be dramatic for high-mass galaxies (Obreschkow & Glazebrook 2014; P18) or bulgeless galaxies in general (El-Badry et al. 2018), it is more accurate to take it into account, specially when dealing with dwarfs. Considering this, in this work we derive V_* using the stellar-asymmetric drift correction as follows.

3.1.1. Stellar-asymmetric drift correction

First, we will consider the circular speed $V_{\rm c}$ of the galaxies. By definition (e.g., Binney & Tremaine 2008), $V_{\rm c}^2 = V_{\rm rot}^2 + V_{\rm AD,gas}^2$, with $V_{\rm AD,gas}^2$ the gas-asymmetric drift correction (e.g., Read et al. 2016; Iorio et al. 2017), a term to correct for pressure-supported motions. For massive galaxies $V_{\rm c}$ is very close to the rotation traced by the gas, $V_{\rm c} \approx V_{\rm rot}$. For the dwarfs the story is different as pressure-supported motions become more important. Therefore, in all our dwarfs the gas-asymmetric drift correction has been applied to obtain $V_{\rm c}$ from $V_{\rm rot}$. Once $V_{\rm c}$ is obtained for all the galaxies, we aim to derive the stellar rotation velocities via the relation $V_*^2 = V_{\rm c}^2 - V_{\rm AD,*}^2$, where $V_{\rm AD*}$ is the stellar asymmetric drift correction.

It can be shown (e.g., Binney & Tremaine 2008; Noordermeer et al. 2008), that for galaxies with exponential density profile the stellar asymmetric drift correction $V_{\rm AD*}$ is given by the expression

$$V_{\rm AD*}^2 = \sigma_{*,\rm R}^2 \left[\frac{R}{R_{\rm d}} - \frac{1}{2}\right] - R\,\frac{{\rm d}\sigma_{*,\rm R}^2}{{\rm d}R}, \tag{2}$$

where $R_{\rm d}$ is the exponential disc scale length, and $\sigma_{*,\rm R}$ the radial component of the stellar velocity dispersion. This expression assumes the anistropy $\sigma_{*,z} = \sigma_{*,\phi} = \sigma_{*,\rm R}/\sqrt{2}$ (e.g., Binney & Tremaine 2008; Noordermeer et al. 2008; Leaman et al. 2012), but we note that P18 found just small differences (less than 10%) if isotropy is assumed.

From theoretical arguments (van der Kruit & Searle 1981; van der Kruit 1988), later confirmed by observations (e.g., Bottema 1993; Swaters 1999; Martinsson et al. 2013, and references therein), the stellar velocity dispersion profile follows an exponential vertical profile of the form

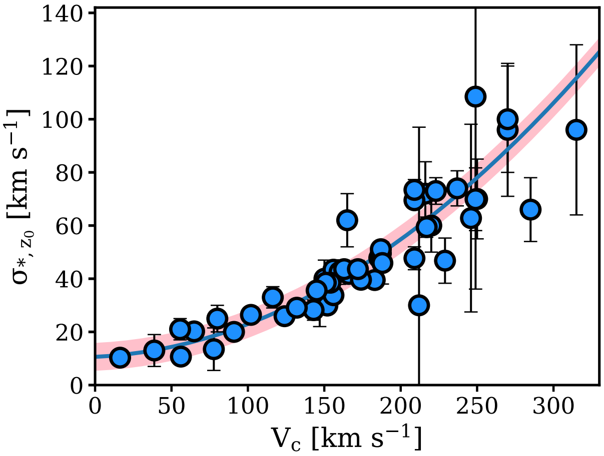

Fig. 2. Relation between the circular speed and the central stellar velocity dispersion in the vertical direction for spiral and dwarf galaxies. Blue points represent the values from a compilation of studies and the blue line and pink band are a fit to the points and its assumed uncertainty, respectively. Not all the galaxies have a reported uncertainty in V_c, so we do not plot any horizontal errorbar for the sake of consistency.

$\sigma_{*,z} = \sigma_{*,z_0}\exp(-R/2R_\mathrm{d})$, although there are not many observational constraints regarding this for the smallest dwarfs (e.g., Hunter et al. 2005; Leaman et al. 2012; Johnson et al. 2015). While we do not know σ_{*,z_0} a priori, different authors have found correlations between σ_{*,z_0} and different galaxy properties, such as surface brightness, absolute magnitude, and circular speed (see for instance Bottema 1993; Martinsson et al. 2013; Johnson et al. 2015).

We exploit the relation between V_c and σ_{*,z_0} to estimate the latter. We compile both parameters for a set of galaxies in the literature, ranging from massive spirals to small dwarf irregulars (Bottema 1993; Swaters 1999; van der Marel et al. 2002; Hunter et al. 2005; Leaman et al. 2012; Martinsson et al. 2013; Johnson et al. 2015; Hermosa Muñoz et al. 2020), as shown in Fig. 2. A second-order polynomial provides a good fit to the points through the relation:

$$\frac{\sigma_{*,z_0}}{\mathrm{km\,s^{-1}}} = 9.7\left(\frac{V_\mathrm{c}}{100\,\mathrm{km\,s^{-1}}}\right)^2 + 2.6\left(\frac{V_\mathrm{c}}{100\,\mathrm{km\,s^{-1}}}\right) + 10.61. \quad (3)$$

We adopt an uncertainty of $\pm 5\,\mathrm{km\,s^{-1}}$ in σ_{*,z_0}, shown as a pink band in Fig. 2, motivated by different tests while fitting the observational points.

Finally, it is also observed (see e.g., Barat et al. 2020 and the previous references) that the stellar velocity dispersion profile rarely goes below 5–10 $\mathrm{km\,s^{-1}}$ even at the outermost radii. Therefore, we set a 'floor' value for the $\sigma_{*,z}$ profile equal to $10\,\mathrm{km\,s^{-1}}$, such that it never goes below this value. With this, we have fully defined $\sigma_{*,z}$, so we can proceed to compute $\sigma_{*,\mathrm{R}}$ and thus $V_{\mathrm{AD}*}$. We note here that adopting a floor value has as the consequence that some dwarfs will have a $\sigma_{*,\mathrm{R}}$ that stays constant at large radii, similar to what has been reported in some observations of dwarf irregulars (e.g., Hunter et al. 2005; van der Marel et al. 2002).

As expected, we find that for massive discs the correction is very small, but it can be more important for less massive galaxies. Figure 3 illustrates this with four examples that demonstrate that while the correction is negligible for the massive spirals, for the dwarfs it is not. For the dwarfs, while the uncertainty in V_* is often consistent with the values of V_c and V_rot, the offset is systematic and important in some cases, highlighting the importance of applying the stellar asymmetric drift correction. For a few dwarf galaxies (DDO 181, DDO 210, DDO 216, NGC 3741, and UGC 07577) the resulting stellar rotation curves are too affected by the correction to be considered reliable: Either they have very large uncertainties such that the stellar rotation curve is compatible with zero at all radii, or it simply goes to zero; the j_* and j_bar of these galaxies are therefore discarded. Further tests on our approach to estimate V_* and its robustness can be found in Appendix B.

3.1.2. Deriving j_bar

Once we estimated j_* after taking into account the stellar asymmetric drift correction, we computed j_bar profiles with the expression

$$j_\mathrm{bar} = f_\mathrm{gas} j_\mathrm{gas} + (1 - f_\mathrm{gas}) j_*, \quad (4)$$

where f_gas is the gas fraction, and with j_gas and j_* computed following Eq. (1). The uncertainty in j_k (with k being stars or gas) is estimated as (e.g., Lelli et al. 2016b; P18):

$$\delta_{j_k} = 2\,R_{\mathrm{c}_k}\sqrt{\frac{1}{N}\sum_i^N \delta^2_{v_i} + \left(\frac{V_\mathrm{f}}{\tan i}\delta_i\right)^2 + \left(V_\mathrm{f}\frac{\delta_\mathrm{D}}{D}\right)^2}, \quad (5)$$

with R_c a characteristic radius (defined below in Eq. (6)), V_f the velocity of the flat part of the rotation curve[1], δ_{v_i} the individual uncertainties in the rotation velocities, i the inclination of the galaxy and δ_i its uncertainty, and D and δ_D the distance to the galaxy and its uncertainty, respectively. In turn, R_c is defined as

$$R_{\mathrm{c}_k} = \frac{\int_0^\mathrm{R} R'^2\,\Sigma_k(R')\,(R')\,\mathrm{d}R'}{\int_0^\mathrm{R} R'\,\Sigma_k(R')\,\mathrm{d}R'}. \quad (6)$$

For an exponential profile, R_c becomes R_d, as used in P18. The uncertainty associated with j_bar comes from propagating the uncertainties in Eq. (4).

We remind the reader that we have accounted for the presence of helium by assuming $M_\mathrm{gas} = 1.33 M_\mathrm{HI}$, and neglecting any input from molecular gas to j_bar or M_bar. This does not affect our analysis in a significant way: In comparison with the H I and stellar components, the contribution of molecular gas to the baryonic mass is marginal (e.g., Catinella et al. 2018; Cimatti et al. 2019, and references therein), and since molecular gas is much more concentrated than the H I, it contributes even less to the final j_bar (e.g., Obreschkow & Glazebrook 2014). In a similar way, we do not attempt to take the angular momentum of the galactic coronae (e.g., Pezzulli et al. 2017) into consideration.

3.2. Convergence criteria

We determined j_gas and j_* by means of Eq. (1); Fig. 4 shows representative examples of j_gas and j_* cumulative profiles. Then, we combined them to obtain j_bar with Eq. (4).

It is important to see whether or not the cumulative profiles converge at the outermost radii because non-converging profiles may lead to a significant underestimation of j. To decide whether or not the cumulative profile of a galaxy (for stars, gas and baryons independently) is converging or not, we proceed as

---

[1] If the rotation curve does not show clear signs of flattening, according to the criterion of Lelli et al. (2016b), we use the outermost measured circular speed.

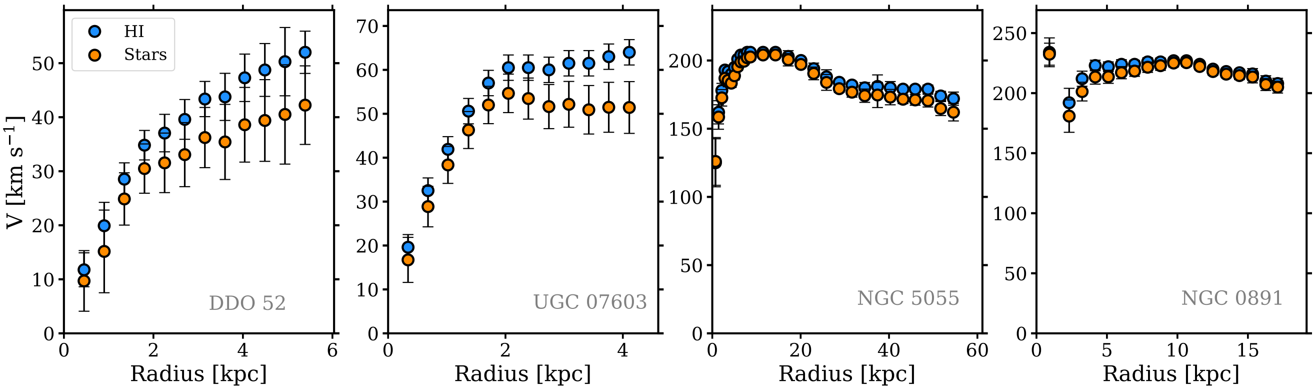

Fig. 3. Gas (blue) and stellar (orange) rotation curves for two dwarf (*left*) and two massive (*right*) galaxies, showing the relative importance of the asymmetric drift correction.

follows. We fit the outer points of the profile with a second-order polynomial $\mathcal{P}$; in practice we fit the outer 20% of the profile or the last four points if the outer 20% of the profile spans only three points, for the sake of robustness in the fit. Then, we extract the value of j at the outermost point of the observed profile, and we compare it with the maximum value that $\mathcal{P}$ would have if extrapolated to infinity. When the ratio $\mathcal{R}$ between these two is 0.8 or larger, we consider the profile as converging. Figure 4 shows representative cases of $j_{\rm gas}$ and j_* cumulative profiles and their corresponding $\mathcal{P}$, exemplifying the cases where the profile has reached the flat part (blue), where it shows signs of convergence (green) and we accept it, and where it is clearly not converging (orchid) and thus is excluded from further analyses.

Our choice of using $\mathcal{R} \geq 0.8$ is empirically driven, and we check its performance as follows. Using about 50 galaxies with clearly convergent j profiles (for instance NGC 7793 in Fig. 4), which have $\mathcal{R} = 1$, we do the following exercise. We remove the outermost point of the cumulative profile, and fit the last 20% of the resulting profile with a new polynomial $\mathcal{P}'$, which then implies a new (lower) $\mathcal{R}'$; this step is repeated until $\mathcal{R}'$ falls to the limit value of 0.8. When this happens, we compare the maximum value of the cumulative profile at the radius where $\mathcal{R}' = 0.8$ with respect to the maximum value of the original ($\mathcal{R} = 1$) profile. Not unexpectedly, these tests reveal that imposing $\mathcal{R} \geq 0.8$ as a convergence criterion allows for a recovery of j with less than 15% of difference with respect to the case where $\mathcal{R} = 1$ in the case of the stars, and less than 20% in the case of the gas. Discrepancies below 20% translate into sub-0.1 dex differences in the final scaling laws. Changing our criterion to a stricter $\mathcal{R} \geq 0.9$ only improves the recovery by ∼5%. Relaxing the criterion to $\mathcal{R} \geq 0.7$ increases the discrepancies by about 5−10%, giving total differences of the order of 0.15 dex. Given this, we adopt $\mathcal{R} \geq 0.8$ as a good compromise, but we notice that using $\mathcal{R} \geq 0.7$ or $\mathcal{R} \geq 0.9$ does not change the nature of the results shown below. This criterion is found to be useful not only because it is simple and applicable to stars, gas, and baryons, but also because it uses all the information in the outer part of the cumulative profile, rather than in the last point only (e.g., P18; Marasco et al. 2019). More information on the effects of changing the required $\mathcal{R}$ can be found in Appendix B.

We visually inspect the cumulative profiles to make sure that our convergence criterion is meaningful for all the galaxies. For the rest of this paper we will analyse only those galaxies whose specific angular momentum cumulative profile meets our convergence criteria, defining in this way our final sample. Table 1 provides the list of galaxies we compiled, giving their mass and specific angular momentum for stars, gas, and baryons, together with the exponential disc scale length and the value of the convergence factor $\mathcal{R}$. According to our criterion discussed above, out of our 157 galaxies, 132 have a convergent j_* profile, 87 a convergent $j_{\rm gas}$, and 106 a convergent $j_{\rm bar}$.

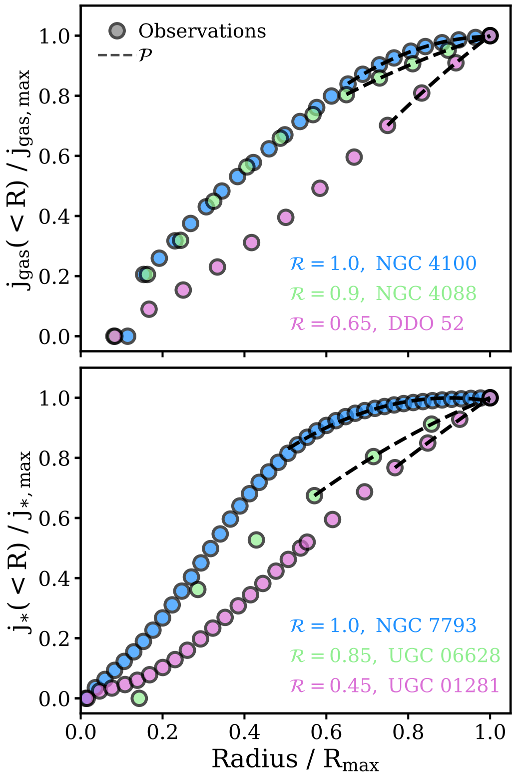

Fig. 4. Example of representative cumulative $j_{\rm gas}$ and j_* profiles in our sample. The axes are normalized to allow the comparison between the profiles. The points show the observed cumulative profiles for the gas (*top*) and stellar (*bottom*) component, while the dashed lines show the fitted polynomial $\mathcal{P}$ to these profiles (see text). The name of the galaxy and the value of the convergence factor $\mathcal{R}$ for their profiles are provided. Only galaxies with $\mathcal{R} \geq 0.8$ are used in our analysis. We note that, due to the normalization, the last point of all the profiles overlap with each other.

The fact that the number of galaxies with converging j_* profiles is larger than the number with converging $j_{\rm gas}$ ones is because Σ_* declines much faster than $\Sigma_{\rm gas}$, such that in outer rings of the rotation curves the contribution from stars is often

Table 1. Main properties of our galaxy sample.

Name	M_*	δM_*	$M_{\rm gas}$	$\delta M_{\rm gas}$	$M_{\rm bar}$	$\delta M_{\rm bar}$	j_*	δj_*	$j_{\rm gas}$	$\delta j_{\rm gas}$	$j_{\rm bar}$	$\delta j_{\rm bar}$	$R_{\rm d}$	$\mathcal{R}_*$ $^{(\dagger)}$	$\mathcal{R}_{\rm gas}$ $^{(\dagger)}$	$\mathcal{R}_{\rm bar}$ $^{(\dagger)}$
	[10^8 $M_\odot$]		[10^8 $M_\odot$]		[10^8 $M_\odot$]		[kpc km s^{-1}]		[kpc km s^{-1}]		[kpc km s^{-1}]		[kpc]			
(1)	(2)	(3)	(4)	(5)	(6)	(7)	(8)	(9)	(10)	(11)	(12)	(13)	(14)	(15)	(16)	(17)
DDO 50	1.80	0.48	7.19	1.34	8.99	1.42	58	26	142	28	126	38	0.90	1.00	0.97	0.97
DDO 52	0.88	0.23	2.44	0.43	3.31	0.48	66	13	153	17	130	31	0.94	0.99	0.70	0.75
DDO 87	0.41	0.26	2.04	1.24	2.44	1.27	83	34	141	53	132	118	1.13	0.25	0.79	0.77
DDO 126	0.33	0.10	1.45	0.31	1.78	0.33	40	20	62	8	58	18	0.82	0.98	0.85	0.88
DDO 133	0.43	0.29	1.16	0.77	1.59	0.82	49	24	65	26	60	54	0.80	0.90	0.92	0.92
DDO 168	0.84	0.22	2.71	0.52	3.55	0.57	64	14	109	13	98	26	1.03	0.99	0.87	0.89
NGC 4639	166.10	45.35	17.01	2.78	183.10	45.43	830	48	1394	70	882	63	1.68	0.99	0.90	0.97
NGC 4725	523.10	144.00	35.08	5.86	558.20	144.10	1914	160	3568	270	2018	170	3.39	1.00	0.98	1.00
NGC 5584	114.40	31.21	22.84	3.73	137.20	31.43	757	77	1022	83	802	89	2.63	0.97	0.93	0.96

Notes. (1) Name. (2) and (3) Stellar mass and uncertainty. (4) and (5) Gas mass and uncertainty. (6) and (7) Baryonic mass and uncertainty. (8) and (9) Stellar specific angular momentum and uncertainty. (10) and (11) Gas specific angular momentum and uncertainty. (12) and (13) Baryonic specific angular momentum and uncertainty. (14) Exponential disc scale length. (15)–(17) Convergence factor for the j_*, $j_{\rm gas}$ and $j_{\rm bar}$ profiles. The complete version of this table is available at the CDS. $^{(\dagger)}$These convergence criteria should be seen as an indication of the convergence of the j profiles rather than taken at face value to predict the exact value of j. In addition to this, values below 0.7 should be taken with extra caution as we find them to be low not necessarily because they are very far from convergence, but because they rely on an extrapolation of a polynomial that it is usually monotonically increasing for those profiles. Along this paper we used $\mathcal{R} \geq 0.8$ to define a j profile as convergent.

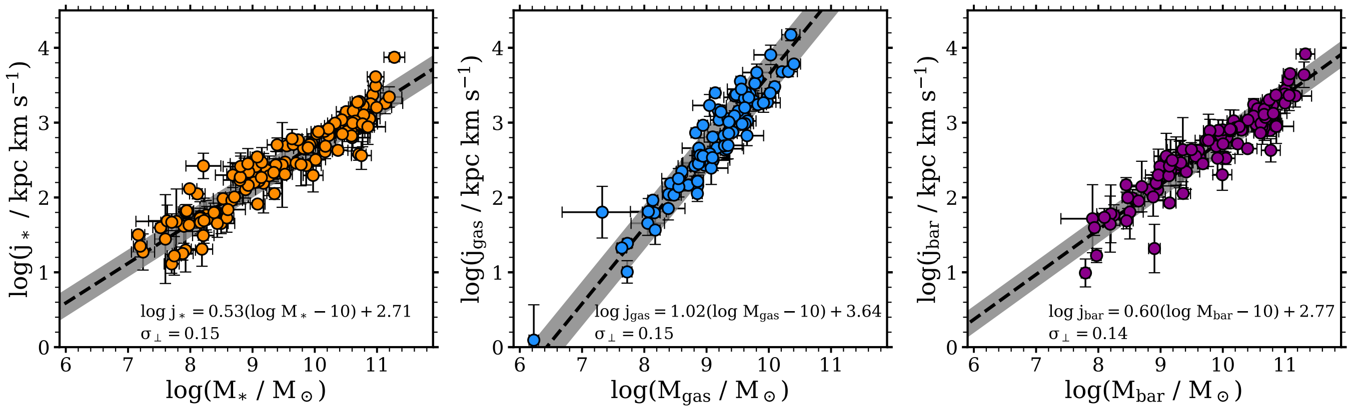

Fig. 5. *From left to right*: stellar, gas, and baryonic j–M relations for our sample of galaxies. In all the panels the circles represent the observed galaxies, while the dashed black line and grey region show, respectively, the best-fitting relations and their perpendicular intrinsic scatter. The three relations are well fitted by unbroken power-laws: The best-fitting relations are shown for each panel (see Table 2). We remind the reader that each panel includes only the galaxies with convergent j_*, $j_{\rm gas}$, and $j_{\rm bar}$ profile, respectively, so the galaxies shown in one panel are not necessarily the same as in the other panels.

negligible. Instead, $\Sigma_{\rm gas}$ is more extended (in fact enough flux to trace the rotation curve is needed), making it harder for its cumulative profile to converge. This is also clear from Fig. 4, where the flattening of the stellar profiles is more evident than for the gas profiles.

Since $j_{\rm bar}$ is not only the sum of j_* and $j_{\rm gas}$ but is weighted by the gas fraction (Eq. (4)), there can be cases where even if one of the two does not converge, $j_{\rm bar}$ does. For example, in a galaxy with a small gas fraction, the convergence of j_* ensures the convergence of $j_{\rm bar}$, regardless of the behaviour of $j_{\rm gas}$. The same can happen for a heavily gas-dominated dwarf with a converging $j_{\rm gas}$ profile. This explains why there are more converging $j_{\rm bar}$ profiles than $j_{\rm gas}$ ones.

4. The stellar, gas, and baryonic specific angular momentum–mass relations for disc galaxies

4.1. The j_*–M_* relation

In the left panel of Fig. 5 we show the j_*–M_* plane for our sample of galaxies. We find a clear power-law relation followed reasonably well by all galaxies. It is particularly tight at the high-mass regime, and the scatter (along with the observational errors) increases when moving towards lower masses; despite this, there is no compelling evidence for a change in the slope of the relation at dwarf galaxy scales.

We fit our points with a power-law of the form

$$\log\left(\frac{j}{\rm kpc\,km\,s^{-1}}\right) = \alpha[\log(M/M_\odot) - 10] + \beta, \tag{7}$$

where in this case $j = j_*$ and $M = M_*$.

We fit Eq. (7) using a likelihood as in P18 and Posti et al. (2019a), which includes a term for the orthogonal intrinsic scatter ($\sigma_\perp$), and we use a Markov chain Monte Carlo approach (Foreman-Mackey et al. 2013) to constrain the parameters after assuming uninformative priors. We find the best-fitting parameters to be $\alpha = 0.53 \pm 0.02$ and $\beta = 2.71 \pm 0.02$, with a perpendicular intrinsic scatter $\sigma_\perp = 0.15 \pm 0.01$. Table 2 provides the coefficients for all the j–M relations found in this work.

Table 2. Coefficients of the best-fitting j–M laws, as shown in Fig. 5, obtained by fitting the observed relations with Eq. (7).

	α	β	$\sigma_\perp$
Stars	0.53 ± 0.02	2.71 ± 0.02	0.15 ± 0.01
Gas	1.02 ± 0.04	3.64 ± 0.03	0.15 ± 0.01
Baryons	0.60 ± 0.02	2.77 ± 0.02	0.14 ± 0.01

4.2. The j_{gas}–M_{gas} relation

The middle panel of Fig. 5 shows the gas specific angular momentum–mass relation. Similarly to the stellar case, the relation of the gas component is also well represented by a simple power-law (Eq. (7)) with best-fitting parameters $\alpha = 1.02 \pm 0.04$, $\beta = 3.64 \pm 0.03$, and $\sigma_\perp = 0.15 \pm 0.01$.

The slope is significantly steeper than for the stars, but the trend is also followed remarkably well by all galaxies. We mainly cover ~3 orders of magnitude in gas mass, $8 \leq \log(M_{\rm gas}/M_\odot) \leq 11$, although we have one galaxy (DDO 210) at $M_{\rm gas} \approx 10^6\,M_\odot$ whose position is perfectly consistent with the $j_{\rm gas}$–$M_{\rm gas}$ sequence of more massive galaxies. Moreover, it is clear that our dwarfs follow the same law as more massive galaxies.

4.3. The j_{bar}–M_{bar} relation

In the right panel of Fig. 5 we show the $j_{\rm bar}$–$M_{\rm bar}$ plane for our sample. The relation looks once more like an unbroken power-law, so we fit the observations with Eq. (7). The best-fitting coefficients are $\alpha = 0.60 \pm 0.02$, $\beta = 2.77 \pm 0.02$, and $\sigma_\perp = 0.14 \pm 0.01$.

The perpendicular intrinsic scatter of the baryonic relation ($\sigma_\perp = 0.14 \pm 0.01$) is consistent with the individual values of the stellar ($\sigma_\perp = 0.15 \pm 0.01$) and gas ($\sigma_\perp = 0.15 \pm 0.01$) relations. This is likely due to the fact that the stellar and gas components dominate at different $M_{\rm bar}$, such that at high $M_{\rm bar}$ the intrinsic scatter of the baryonic relation is set by the intrinsic scatter of j_*–M_* relation, while at the low $M_{\rm bar}$ it is the scatter of the $j_{\rm gas}$–$M_{\rm gas}$ relation the one that dominates.

One of the most important results drawn from the baryonic relation in Fig. 5 is that the most massive spirals and the smallest dwarfs in our sample lie along the same relation. We discuss this in more detail in Sect. 5.3.

In addition to our fiducial best-fitting parameters given above, we performed the exercise of building the $j_{\rm bar}$–$M_{\rm bar}$ relation using only the 77 galaxies that have both a convergent j_* and $j_{\rm gas}$ profile, instead of the 104 galaxies with converging $j_{\rm bar}$ profile but without necessarily having both convergent j_* and $j_{\rm gas}$ profiles (see Sect. 3.2). The best-fitting parameters for Eq. (7) using this subsample are $\alpha = 0.56 \pm 0.02$, $\beta = 2.87 \pm 0.02$, and $\sigma_\perp = 0.11 \pm 0.01$. This slope is consistent with the fiducial slope derived with our convergence criteria within their uncertainties, and the intercept changes by only ~0.1 dex. Also, not unexpectedly, the intrinsic scatter is slightly reduced. In this subsample, however, the low-mass regime is significantly reduced, especially below $M_{\rm bar} < 10^{9.5}\,M_\odot$.

5. Discussion

In Sect. 4 we showed and described the stellar and gas j–M relations, which are then used to derive the $j_{\rm bar}$–$M_{\rm bar}$ relation. Empirically, the three laws are well characterized by unbroken linear relations (in log-log space, see Eq. (7)). While there are no clear features indicating breaks in the relations, we statistically test this possibility by fitting the j–M laws with double power-laws. The resulting best-fitting double power-laws are largely indistinguishable from the unbroken power-laws within our observed mass ranges. Moreover, the linear models are favoured over the double power-law models by the Akaike information criterion (AIC) and the Bayesian information criterion (BIC). Compared to the values obtained for the single power-law, the AIC and BIC of the broken power-law fit are larger by 7 and 12, respectively, in the case of the stellar relation, by 5 and 10 for the gas, and by 6 and 11 for the baryons. Having established that the single power-laws provide an appropriate fit to the observed j–M planes, in the following subsections we discuss some similarities and discrepancies between our results and previous works, as well as other further considerations regarding the phenomenology of these laws.

5.1. Comparison with previous works

5.1.1. j_*–M_* relation

The stellar specific angular momentum–mass relation for disc galaxies has been recently reviewed and refined by P18. An important result that they show, is that while some galaxy formation models (e.g., Obreja et al. 2016) predict a break or flattening in the j_*–M_* law at the low-mass end, the observational relation is an unbroken power-law from the most massive spiral galaxies to the dwarfs. While there is evidence for this in Fig. 2 of P18, their sample has very few objects with $M_* < 10^{8.5}\,M_\odot$, a fact that may pose doubts on the supposedly unbroken behaviour of the relation. Our sample largely overlaps with the sample of P18 who used the SPARC compilation, but importantly, as described in Sect. 2, it also includes dwarf galaxies from LITTLE THINGS, LVHIS, VLA-ANGST, and WHISP, adding several more galaxies with $M_* < 10^{8.5}\,M_\odot$, and allowing us to set strong constraints on the relation at the low-mass regime. As mentioned before, we find a similar behaviour as the one reported by P18: Dwarf and massive disc galaxies lie in the same scaling law.

P18 report very similar values to ours (see also Fall 1983; Romanowsky & Fall 2012; Fall & Romanowsky 2013; Cortese et al. 2016). Those authors find $\alpha = 0.55 \pm 0.02$ and $\sigma_\perp = 0.17 \pm 0.01$; the parametrization used to derive their intercept $\beta = 3.34 \pm 0.03$ is different than that used in Eq. (7), but close to ours (0.1 dex higher) once this is taken into account. Therefore, our values are in very good agreement with recent determinations of the j_*–M_* relation, with the advantage of a better sampling at the low-M_* regime. We also notice that despite including more dwarfs (~35, those from LITTLE THINGS, LVHIS, WHISP, and VLA-ANGST), which increase the observed scatter at the low-M_* regime, we find a slightly smaller global intrinsic scatter.

5.1.2. j_{gas}–M_{gas} relation

The slope that we find for the $j_{\rm gas}$–$M_{\rm gas}$ plane ($\alpha = 1.02 \pm 0.04$) is about two times the value of the slope of the stellar relation ($\alpha = 0.53 \pm 0.02$). It is also steeper than the slope of 0.8 ± 0.08 reported in Kurapati et al. (2018; see also Cortese et al. 2016). Nevertheless, those authors analyzed galaxies with $M_{\rm gas} < 10^{9.5}\,M_\odot$, for which the individual values of their $j_{\rm gas}$ estimates compare well with ours as their points lie within the scatter of ours. Therefore, the differences in the slope reported by Kurapati et al. (2018) and ours are seemingly due to the shorter mass span of their sample: Once galaxies with $6 \leq \log(M_{\rm gas}/M_\odot) \leq 11$ are put together, a global and steeper slope close to 1 emerges. Chowdhury & Chengalur (2017) and Butler et al. (2017) do not report the value of their slopes, but as it happens with the sample from Kurapati et al. (2018), the majority of their galaxies lie within the scatter of our larger sample, and some of them are actually included in our sample.

5.1.3. $j_{\rm bar}$–$M_{\rm bar}$ relation

Our best-fitting slope for the $j_{\rm bar}$–$M_{\rm bar}$ law is 0.60 ± 0.02. This is comparable to the value of 0.62 ± 0.02 reported by Elson (2017), and significantly lower than the value of 0.94 ± 0.05 from Obreschkow & Glazebrook (2014; this for bulgeless galaxies, see Chowdhury & Chengalur 2017), and than the value of 0.89 ± 0.05 from Kurapati et al. (2018). It is important, however, to bear in mind that the sample from Obreschkow & Glazebrook (2014) consists mainly of massive spirals, and the sample from Kurapati et al. (2018) consists of dwarfs only, so the differences are at least partially explained by the fact that we explore a broader mass range.

Very recently, Murugeshan et al. (2020) reported a slope of 0.55 ± 0.02 for a sample of 114 galaxies. Their slope is slightly shallower but nearly statistically compatible with our value once both $1\sigma_\perp$ uncertainties are taken into account. They do not report the value of their intercept, but based on the inspection of their Fig. 3 we find it also in agreement with ours. Nevertheless, there are some differences in our analysis with respect to theirs. For instance, our mass coverage at $M_{\rm bar} < 10^9\,M_\odot$ is a bit more complete (11 galaxies in their work vs 23 in our convergent sample), and, very importantly, we applied a converge criterion to all our sample in order to select only the most accurate j profiles. In addition to this, while both studies use near infrared luminosities to trace M_* (mostly 3.6 μm in our case, and 2.2 μm for Murugeshan et al. 2020), we use a Υ that has been found to reduce the scatter in scaling relations that depend on M_* such as the baryonic Tully–Fisher relation (see Lelli et al. 2016b), while the calibration used by Murugeshan et al. (2020) may have a larger scatter, up to one order of magnitude in M_* at given infrared luminosity (Wen et al. 2013). Finally, we determine V_* instead of assuming co-rotation of gas and stars, although this does not play an important role when determining the global $j_{\rm bar}$–$M_{\rm bar}$ relation (cf. Appendix B).

Despite these differences, which may lead to discrepancies on a galaxy by galaxy basis, the slopes between both works are statistically in agreement. Murugeshan et al. (2020) mention that it is likely that their slope is slightly biased towards flatter values given their lack of galaxies with $M_{\rm bar} < 10^9\,M_\odot$. For our sample, which extends towards lower masses, the slope is marginally steeper, in agreement with the reasoning of Murugeshan et al. (2020).

5.2. *Residuals and internal correlations*

In this section we explore whether or not the j–M relations correlate with third parameters. We show in Fig. 5 that the three j–M relations are well described by unbroken power-laws. Yet, this does not necessarily imply that there are no systematic residuals as a function of mass or other physical parameters.

To explore this possibility, in Fig. 6 we look at the difference between the measured j of each galaxy and the expected $j_{\rm fit}$ according to the best-fitting power-law we found previously, as a function of M. The first conclusion we reach from this figure is that there does not seem to be any systematic trend of the residuals for the stellar and gas relations as a function of M_* or $M_{\rm gas}$, respectively: within the scatter of our data, a galaxy is equally likely to be above or below the best-fitting relations. The scenario seems to be different for the baryonic relation (bottom panels in Fig. 6), where galaxies with higher baryonic masses tend to scatter below the best-fitting relation while less massive galaxies tend to scatter above it. This is the result of a correlation with the gas fraction, as we discuss later in Sect. 5.2.2.

To further study the behaviour of the residuals from the best-fitting relations and identify parameters correlated with such residuals, we look at internal correlations with other quantities. For instance, given the dependence of $j_{\rm bar}$ on $f_{\rm gas}$ (Eq. (4)), $f_{\rm gas}$ is an interesting parameter to explore within the j–M relations. The same happens with $R_{\rm d}$, given the relation between the spin parameter λ of dark matter haloes and $R_{\rm d}$ (e.g., Mo et al. 1998; Posti et al. 2019a; Zanisi et al. 2020), and that for galaxy discs with Sérsic profiles and flat rotation curves $j_* \propto R_{\rm d}$ (Romanowsky & Fall 2012). As shown in Fig. 6, there are internal correlations with both parameters, which we briefly describe here.

5.2.1. Disc scale length

In the case of the disc scale length as a third parameter, Fig. 6 (left panels) encodes also the well-known M_*–$R_{\rm d}$ relation: More massive galaxies have more extended optical disc scale length, although the scatter is relatively large at given M_* (e.g., Fernández Lorenzo et al. 2013; Cebrián & Trujillo 2014; Lange et al. 2015). Nonetheless, the figure also shows other trends at fixed mass.

At fixed M_* (upper left panel), galaxies with a higher than average j_* have a larger $R_{\rm d}$. This is not surprising given Eq. (1) (see also Romanowsky & Fall 2012), but it is still interesting to show the precise behaviour of this correlation across nearly five orders of magnitude in mass. The trend is not clearly visible in the gas relation (mid left panel), which is not unexpected given the less clear interplay between $R_{\rm d}$ and $j_{\rm gas}$ (as opposed to j_*), and the scattered relation between $R_{\rm d}$ and the size of the gaseous disc (e.g., Lelli et al. 2016a). The inspection of the $j_{\rm bar}$–$M_{\rm bar}$ plane (lowermost left panel) reveals that the trend of high-j galaxies having larger $R_{\rm d}$ at fixed $M_{\rm bar}$ is visible at the high-mass regime (where the stellar relation dominates), but becomes less evident at low masses (where the gas relation is dominant).

5.2.2. Gas fraction

The right hand side panels of Fig. 6 show the vertical residuals from the j–M laws adding the gas fraction as a third parameter. Trends also seem to emerge in these cases. In general, the relation between mass and gas fraction (e.g., Huang et al. 2012; Catinella et al. 2018) is clear: More massive galaxies have lower $f_{\rm gas}$ on average (see also Fig. 1).

From the j_*–M_* relation, we can see that at fixed M_* galaxies with higher $f_{\rm gas}$ have larger j_* than galaxies with lower $f_{\rm gas}$. Results along the same lines were reported by Huang et al. (2012) using unresolved ALFALFA observations (Haynes et al. 2011), by Lagos et al. (2017) analysing hydrodynamical simulations, and by e.g., Stevens et al. (2018), Zoldan et al. (2018), and Irodotou et al. (2019) using semi-analytic models.

The above trend is inverted in the case of the gas: At fixed $M_{\rm gas}$ disc galaxies with lower gas content have higher $j_{\rm gas}$. This is perhaps due to the fact that the fuel for star formation is the

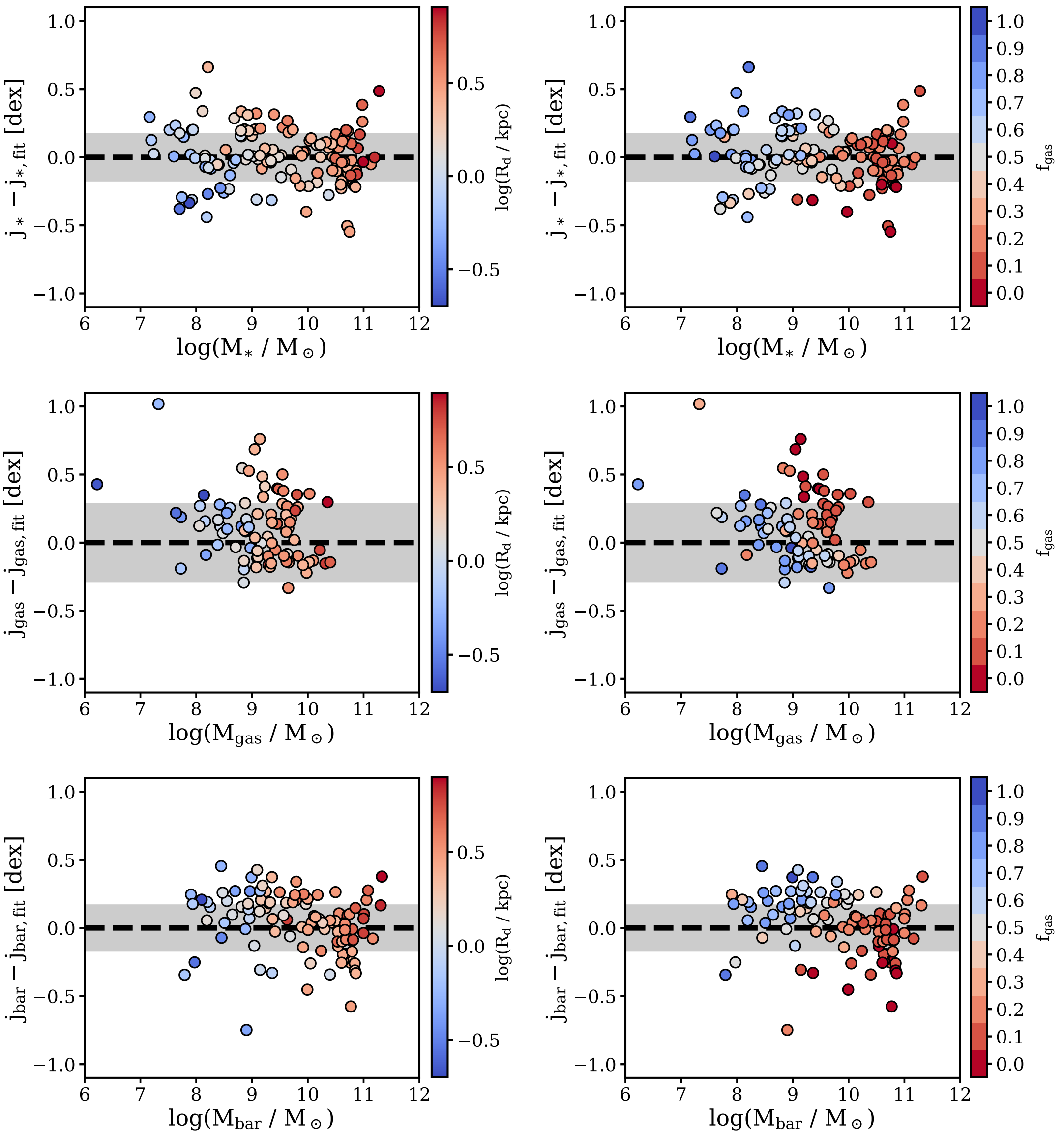

Fig. 6. Residuals from the best-fitting j–M laws at fixed M. The case of no offset from the best-fitting relation is represented with a dashed black line, while the grey band shows the scatter of the relation. *Left* and *right panels* include, respectively, the disc scale length (see Table 1) and the gas fraction as colour-coded third parameters. The main conclusions from this figure are that at fixed M_* galaxies with a higher j_* have larger R_{d}, and at fixed M_{bar} galaxies with lower f_{gas} have a lower j_{bar}.

low-j gas, so the remaining gas reservoirs of gas-poor galaxies effectively see an increase in its j_{gas} (see also Lagos et al. 2017; Zoldan et al. 2018).

That gas-poor galaxies have higher j_{gas} may also be related with the H I surface density profile of galaxies. At fixed M_{gas} galaxies with low f_{gas} have higher M_*, and galaxies with high M_* often present a central depression in their H I distribution (e.g., Swaters 1999; Martinsson et al. 2016, and references therein). At fixed M_{gas} the central depression implies that the mass distribution is more extended, and so j_{gas} should be larger, as we find in our observational result (see also Murugeshan et al. 2019).

Lastly, we inspect the residuals for the baryonic relation (bottom right panel of Fig. 6). At fixed M_{bar} galaxies with lower f_{gas} have a lower j_{bar}. This is line with both Eq. (4) and the fact that across all our observed mass regime $j_{\mathrm{gas}} > j_*$: at fixed M_{bar}, gas-poor galaxies have a smaller contribution from j_{gas}, which is larger than j_*. By adding f_{gas} directly into the j_{bar}–M_{bar} plane in Fig. 7 we notice that gas-rich and gas-poor galaxies seem to follow relations with similar slopes but slightly different intercepts, with the intercept of gas-rich galaxies being higher. In fact, the galaxies that fall below the main baryonic relation in Figs. 5 and 6 are mostly those with very low f_{gas} for their M_{bar}.

Murugeshan et al. (2020) studied the j_{bar}–M_{bar} relation dividing their galaxies in two groups: those with near neighbours and those relatively more isolated. They find that at the high-mass end, galaxies with close neighbours tend to have lower j_{bar} than expected, and they suggest that this is likely to be the result of past or present interactions that lowered j_{bar} (see also Lagos et al. 2017). However, somewhat surprisingly, those authors find no significant differences in j_{bar} as a function of the second nearest-neighbour density (see their Fig. 5). We do not segregate our galaxies in terms of isolation, but we find that those with lower j_{bar} are those that show a low f_{gas}.

Some authors have also discussed the relation of f_{gas} with j_{bar} via the stability parameter $q = j_{\mathrm{bar}}\sigma/GM_{\mathrm{bar}}$, with σ the H I velocity dispersion and G the gravitational constant (see

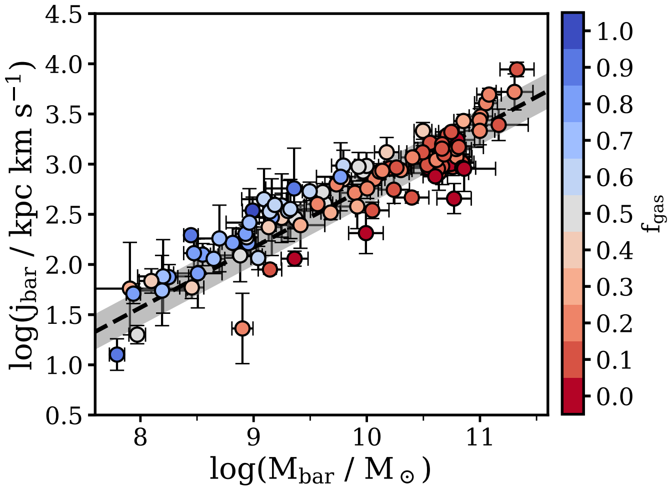

Fig. 7. Baryonic j–M relation colour-coding the galaxies according to their gas fraction. Gas-rich galaxies seem to have a slightly higher intercept than gas-poor ones.

Obreschkow et al. 2016; Lutz et al. 2018; Stevens et al. 2018; Murugeshan et al. 2020). According to them (see also Romeo 2020), at fixed $M_{\rm bar}$ a galaxy with higher $j_{\rm bar}$ has a higher q, meaning that it is more stable against gravitational collapse. On the other hand, galaxies with low-$j_{\rm bar}$ form stars more efficiently as they are less stable. In principle, the bottom right panel of Fig. 6 seems in line with their expectations, as $f_{\rm gas}$ increases with positive $j_{\rm bar}-j_{\rm bar,fit}$, although discussion exists in the literature regarding whether or not star formation is primarily regulated by angular momentum and disc stability, or, for instance, by gas cooling or gas volume density (e.g., Leroy et al. 2008; Obreschkow et al. 2016; Bacchini et al. 2019). A deeper investigation on how j, M, and $f_{\rm gas}$ intertwine together will be provided in a forthcoming work (Mancera Piña et al., in prep.).

5.3. The specific angular momentum of dwarf galaxies

Our results on the j_*-M_* plane provide further support to the conclusions from P18 that dwarfs and massive spirals seemingly follow the same scaling law. There are no features in our measurements suggesting a break, although the scatter seems larger at the low-mass end.

Another result we find is that dwarf galaxies fall in the same baryonic (and gas) sequence that describes more massive galaxies well. Results along the same line were reported by Elson (2017), but for a smaller sample and relying on extrapolations of the rotation curves. These findings seem in tension with the results from Chowdhury & Chengalur (2017), Butler et al. (2017), and Kurapati et al. (2018), who concluded that dwarfs have a higher $j_{\rm bar}$ than expected from an extrapolation of the relation for massive spirals. However, this is due to the fact that those authors were comparing their data with the relation found by Obreschkow & Glazebrook (2014), which has a very steep slope and thus tends to progressively underestimate $j_{\rm bar}$ at low $M_{\rm bar}$. As mentioned above, their dwarf galaxies lie close to our dwarfs in the $j_{\rm bar}-M_{\rm bar}$ plane.

In order to explain the idea of dwarfs having a higher $j_{\rm bar}$ than expected, Chowdhury & Chengalur (2017) and Kurapati et al. (2018) discussed two main possibilities: That the higher $j_{\rm bar}$ is a consequence of feedback processes that remove a significant amount of low-j gas, or that it is due to a significantly higher 'cold' gas accretion (see for instance Sancisi et al. 2008; Kereš et al. 2009) in dwarfs than in other galaxies. Kurapati et al. (2018), with similar results as Chowdhury & Chengalur (2017), already discussed that the former scenario is unlikely given the unrealistically high mass-loading factors that would be required, but they left open the possibility of the cold gas accretion. In this context, our results would suggest that these mechanisms are not needed to be particularly different in dwarfs compared with massive spirals as both group of galaxies lie in the same sequence; instead, they suggest that feedback and accretion processes act in a rather continuous way as a function of mass. This seems in agreement with the results we show in Sect. 5.4 regarding the retained fraction of angular momentum.

5.4. The retained fraction of angular momentum

In a ΛCDM context, the angular momentum of both dark matter and baryons is acquired by tidal torques (Peebles 1969). Considering the link between the specific angular momentum of the dark matter halo and its halo mass ($j_{\rm h} \propto \lambda M_{\rm h}^{2/3}$), the baryonic specific angular momentum is given by the expression (see e.g., Fall 1983; Romanowsky & Fall 2012; Obreschkow & Glazebrook 2014; P18)

$$\frac{j_{\rm bar}}{10^3\ {\rm kpc\,km\,s^{-1}}} = 1.96\,\lambda\, f_{j,{\rm bar}}\, f_{\rm M,bar}^{-2/3} \left(\frac{M_{\rm bar}}{10^{10}\ M_\odot}\right)^{2/3}, \tag{8}$$

with λ the halo spin parameter, $f_{j,{\rm bar}}$ the retained fraction of angular momentum ($j_{\rm bar}/j_{\rm h}$), and $f_{\rm M,bar}$ the global galaxy formation efficiency or baryonic-to-halo mass ratio ($M_{\rm bar}/M_{\rm h}$).

Since λ is a parameter that is relatively well known from simulations ($\lambda \approx 0.035$, largely independent of halo mass, redshift, morphology and environment, e.g., Bullock et al. 2001; Macciò et al. 2008), if the individual values of $M_{\rm h}$ were known, it would then be possible to measure $f_{j,{\rm bar}}$ for each individual galaxy.

Despite not knowing the precise value of $M_{\rm h}$ for all our galaxies, we can still investigate the behaviour of $f_{j,{\rm bar}}$ in a statistical way. For this, we can assume a stellar-to-halo mass relation to then find which value of $f_{j,{\rm bar}}$, as a function of mass, better reproduces the observed $j_{\rm bar}-M_{\rm bar}$ relation. We adopt the empirical stellar-to-halo mass relation for disc galaxies recently derived by Posti et al. (2019a), by using accurate mass-decomposition models of SPARC and LITTLE THINGS galaxies (see also Read et al. 2017). The relation from Posti et al. (2019a) follows a single power-law at all masses and deviates from relations derived with abundance matching especially at the high-mass end, where the abundance-matching relations would predict a break at around $M_{\rm h} \sim 10^{12}\ M_\odot$ (e.g., Wechsler & Tinker 2018). As discussed in detail in Posti et al. (2019a,b), such an unbroken relation provides a better fit for disc galaxies.

Going back to Eq. (8), we explore two simple scenarios: One where the retained fraction of angular momentum is constant, $f_{j,{\rm bar}} = f_0$, and one where it is a simple function of $M_{\rm bar}$, $\log f_{j,{\rm bar}} = \alpha \log(M_{\rm bar}/M_\odot) + f_1$, and we fit Eq. (8) for both of them. In the case of the constant retained fraction, we find $f_{j,{\rm bar}} = f_0 = 0.62$. The relation obtained by fixing this value in Eq. (8) is shown in Fig. 8 (solid red line), compared with the observational points. It is clear that the constant $f_{j,{\rm bar}}$ well reproduces the observed relation. In the case where $f_{j,{\rm bar}}$ is a function of $M_{\rm bar}$, the best-fitting coefficients are $\alpha = 0.04$ and $f_1 = -0.62$, and the resulting relation is shown in Fig. 8 with a dashed blue line.

Both scenarios for $f_{j,{\rm bar}}$ fit the data equally well, but the fit with a constant $f_{j,{\rm bar}}$ (having only one free parameter) is favoured

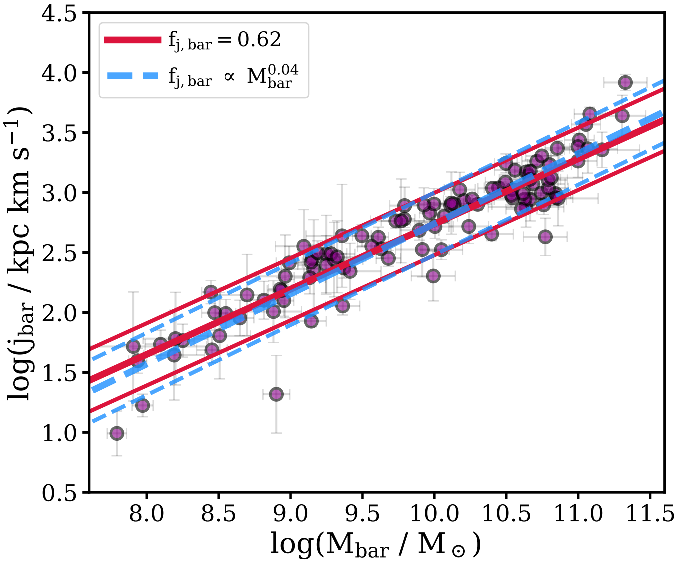

Fig. 8. Observed $j_{\rm bar}$–$M_{\rm bar}$ plane (magenta points) compared with the outcome from Eq. (8) after assuming a constant (solid red line) or mass-dependent (dashed blue line) $f_{j,\rm bar}$. The lines below and above each relation show their scatter, coming from the scatter on λ and on the stellar-to-halo mass relation.

by the BIC and AIC criteria. We also notice that the scatter in the relation can be almost entirely attributed to the scatter on λ (0.25 dex, Macciò et al. 2008) and on the stellar-to-halo mass relation (0.07 dex, Posti et al. 2019a), without significant contribution from the scatter in $f_{j,\rm bar}$.

This provides observational evidence that despite different processes of mass and specific angular momentum gain and loss, the baryons in present-day disc galaxies have 'retained' a high fraction of the specific angular momentum of the haloes, as required by early and recent models of galaxy formation (e.g., Fall & Efstathiou 1980; Fall 1983; Mo et al. 1998; Navarro & Steinmetz 2000; van den Bosch et al. 2001; Fall & Romanowsky 2013; Desmond & Wechsler 2015; Posti et al. 2018b; Irodotou et al. 2019). Our constant value for $f_{j,\rm bar}$ is somewhat smaller than predicted in some cosmological hydrodynamical simulations (e.g., Genel et al. 2015; Pedrosa & Tissera 2015), but it seems to be in good agreement with the outcome of the models from Dutton & van den Bosch (2012), once we account for the different assumptions in the stellar-to-halo mass relation.

As mentioned in the above references (see also Lagos et al. 2017; Cimatti et al. 2019), there are a number of reasons of why $f_{j,\rm bar}$ may be smaller or larger than 1. These include rather complex relations between biased cooling of baryons, angular momentum transfer from baryons to the dark halo via dynamical friction, feedback processes and past mergers. Thus, it remains somewhat surprising that despite all of these complexities, disc galaxies still find a way to inherit their most basic properties (mass and angular momentum) from their parent dark matter haloes in a rather simple fashion.

6. Conclusions

Using a set of high-quality rotation curves, H I surface density profiles, and near-infrared stellar profiles, we homogeneously studied the stellar, gas, and baryonic specific angular momentum–mass laws. Our sample (Fig. 1), representative of dwarf and massive regularly rotating disc galaxies, extends about five orders of magnitude in mass and four in specific angular momentum, providing the largest sample (in number and dynamic range) for which the three relations have been studied homogeneously. The specific angular momentum has been determined in a careful way, correcting the kinematics for both pressure-supported motions and stellar asymmetric drift (e.g., Fig. 3) and checking the individual convergence of each galaxy (Fig. 4).

Within the scatter of the data, the three relations can be characterized by unbroken power-laws (linear fits in log-log space) across all the mass range (Fig. 5), with dwarf and big spiral galaxies lying along the same relations. The stellar relation holds at lower masses than reported before, with a similar slope ($\alpha = 0.53$) and intrinsic scatter ($\sigma_\perp = 0.15$) as reported in previous literature. The gas relation has a slope about two times steeper ($\alpha = 1.02$) than the stellar slope and with a higher intercept. The baryonic relation has a slope $\alpha = 0.60$, relatively close to the value of the slope of the stellar relation, and it also has a similar intrinsic scatter as the stellar and gas j–M laws ($\sigma_\perp = 0.14$). We provide the individual values of the mass and specific angular momentum for our galaxies (Table 1) as well as the best-fitting parameters for the three j–M relations (Table 2).

The three laws also show some dependence on the optical disc scale length $R_{\rm d}$ and the gas fraction $f_{\rm gas}$. The clearest trends are that at fixed M_* galaxies with higher j_* have larger $R_{\rm d}$, while at fixed $M_{\rm bar}$ galaxies with lower $f_{\rm gas}$ have lower $j_{\rm bar}$ (Figs. 6 and 7).

When compared with theoretical predictions from ΛCDM, the $j_{\rm bar}$–$M_{\rm bar}$ scaling relation can be used to estimate the retained fraction of baryonic specific angular momentum, $f_{j,\rm bar}$. We find that a constant $f_{j,\rm bar} = 0.62$ reproduces well the $j_{\rm bar}$–$M_{\rm bar}$ law, with little requirement for scatter in $f_{j,\rm bar}$ (Fig. 8). In general, this provides empirical evidence of a relatively high ratio between the baryonic specific angular momentum in present-day disc galaxies, and the specific angular momentum of their parent dark matter halo. Overall, our results provide important constraints to (semi) analytic and numerical models of the formation of disc galaxies in a cosmological context. They are key for pinning down which physical processes are responsible for the partition of angular momentum into the different baryonic components of discs.

Acknowledgements. We thank Michael Fall for providing insightful comments on our manuscript. The suggestions from an anonymous referee, which helped to improve our paper, were also very much appreciated. We thank Anastasia Ponomareva, Enrico Di Teodoro, Bob Sanders, Rob Swaters, Hong-Xin Zhang, Tye Young, Helmut Jerjen, and Thijs van der Hulst for their help at gathering the data needed for this work. P.E.M.P. would like to thank Andrea Afruni and Cecilia Bacchini for useful discussions. P.E.M.P., F.F., and T.O. are supported by the Netherlands Research School for Astronomy (Nederlandse Onderzoekschool voor Astronomie, NOVA), Phase-5 research programme Network 1, Project 10.1.5.6. L.P. acknowledges support from the Centre National d'Études Spatiales (CNES). E.A.K.A. is supported by the WISE research programme, which is financed by the Netherlands Organization for Scientific Research (NWO). We have used extensively SIMBAD and ADS services, as well the Python packages NumPy (Oliphant 2007), Matplotlib (Hunter 2007), SciPy (Virtanen et al. 2020), Astropy (Astropy Collaboration 2018), and LMFIT (Newville et al. 2014), for which we are thankful.

References

Astropy Collaboration (Price-Whelan, A. M., et al.) 2018, AJ, 156, 123
Bacchini, C., Fraternali, F., Iorio, G., & Pezzulli, G. 2019, A&A, 622, A64
Barat, D., D'Eugenio, F., Colless, M., et al. 2020, MNRAS, 498, 5885
Battaglia, G., Fraternali, F., Oosterloo, T., & Sancisi, R. 2006, A&A, 447, 49
Begeman, K. G. 1987, PhD Thesis, Kapteyn Astronomical Institute, University of Groningen, The Netherlands

Begum, A., & Chengalur, J. N. 2004, A&A, 424, 509
Binney, J., & Tremaine, S. 2008, Galactic Dynamics: Second Edition (Princeton: Princeton University Press)
Boomsma, R. 2007, PhD Thesis, Kapteyn Astronomical Institute, University of Groningen
Bottema, R. 1993, A&A, 275, 16
Bouquin, A. Y. K., Gil de Paz, A., Muñoz-Mateos, J. C., et al. 2018, ApJS, 234, 18
Bullock, J. S., Kolatt, T. S., Sigad, Y., et al. 2001, MNRAS, 321, 559
Butler, K. M., Obreschkow, D., & Oh, S.-H. 2017, ApJ, 834, L4
Catinella, B., Saintonge, A., Janowiecki, S., et al. 2018, MNRAS, 476, 875
Cebrián, M., & Trujillo, I. 2014, MNRAS, 444, 682
Chowdhury, A., & Chengalur, J. N. 2017, MNRAS, 467, 3856
Cimatti, A., Fraternali, F., & Nipoti, C. 2019, Introduction to Galaxy Formation and Evolution: From Primordial Gas to Present-Day Galaxies (Cambridge: Cambridge University Press)
Cortese, L., Fogarty, L. M. R., Bekki, K., et al. 2016, MNRAS, 463, 170
Dalcanton, J. J., Spergel, D. N., & Summers, F. J. 1997, ApJ, 482, 659
Dalcanton, J. J., Williams, B. F., Seth, A. C., et al. 2009, ApJS, 183, 67
de Blok, W. J. G., Walter, F., Brinks, E., et al. 2008, AJ, 136, 2648
Desmond, H., & Wechsler, R. H. 2015, MNRAS, 454, 322
Di Teodoro, E. M., & Fraternali, F. 2015, MNRAS, 451, 3021
D'Onghia, E., Burkert, A., Murante, G., & Khochfar, S. 2006, MNRAS, 372, 1525
Dutton, A. A., & van den Bosch, F. C. 2012, MNRAS, 421, 608
El-Badry, K., Quataert, E., Wetzel, A., et al. 2018, MNRAS, 473, 1930
Elson, E. C. 2017, MNRAS, 472, 4551
Fall, S. M. 1983, in Internal Kinematics and Dynamics of Galaxies, ed. E. Athanassoula, IAU Symp., 100, 391
Fall, S. M., & Efstathiou, G. 1980, MNRAS, 193, 189
Fall, S. M., & Romanowsky, A. J. 2013, ApJ, 769, L26
Fall, S. M., & Romanowsky, A. J. 2018, ApJ, 868, 133
Fernández Lorenzo, M., Sulentic, J., Verdes-Montenegro, L., & Argudo-Fernández, M. 2013, MNRAS, 434, 325
Foreman-Mackey, D., Hogg, D. W., Lang, D., & Goodman, J. 2013, PASP, 125, 306
Fraternali, F., van Moorsel, G., Sancisi, R., & Oosterloo, T. 2002, AJ, 123, 3124
Fraternali, F., Sancisi, R., & Kamphuis, P. 2011, A&A, 531, A64
Genel, S., Fall, S. M., Hernquist, L., et al. 2015, ApJ, 804, L40
Governato, F., Willman, B., Mayer, L., et al. 2007, MNRAS, 374, 1479
Haynes, M. P., Giovanelli, R., Martin, A. M., et al. 2011, AJ, 142, 170
Hermosa Muñoz, L., Taibi, S., Battaglia, G., et al. 2020, A&A, 634, A10
Huang, S., Haynes, M. P., Giovanelli, R., & Brinchmann, J. 2012, ApJ, 756, 113
Hunter, J. D. 2007, Comput. Sci. Eng., 9, 90
Hunter, D. A., Rubin, V. C., Swaters, R. A., Sparke, L. S., & Levine, S. E. 2005, ApJ, 634, 281
Hunter, D. A., Ficut-Vicas, D., Ashley, T., et al. 2012, AJ, 144, 134
Iorio, G., Fraternali, F., Nipoti, C., et al. 2017, MNRAS, 466, 4159
Irodotou, D., Thomas, P. A., Henriques, B. M., Sargent, M. T., & Hislop, J. M. 2019, MNRAS, 489, 3609
Johnson, M. C., Hunter, D., Wood, S., et al. 2015, AJ, 149, 196
Kamphuis, P., Józsa, G. I. G., Oh, S.-H., et al. 2015, MNRAS, 452, 3139
Karachentsev, I. D., Tully, R. B., Dolphin, A., et al. 2007, AJ, 133, 504
Kereš, D., Katz, N., Fardal, M., Davé, R., & Weinberg, D. H. 2009, MNRAS, 395, 160
Kirby, E. M., Jerjen, H., Ryder, S. D., & Driver, S. P. 2008, AJ, 136, 1866
Kirby, E. M., Koribalski, B., Jerjen, H., & López-Sánchez, Á. 2012, MNRAS, 420, 2924
Koribalski, B. S., Wang, J., Kamphuis, P., et al. 2018, MNRAS, 478, 1611
Kulier, A., Galaz, G., Padilla, N. D., & Trayford, J. W. 2020, MNRAS, 496, 3996
Kurapati, S., Chengalur, J. N., Pustilnik, S., & Kamphuis, P. 2018, MNRAS, 479, 228
Lagos, C. D. P., Theuns, T., Stevens, A. R. H., et al. 2017, MNRAS, 464, 3850
Lagos, C. D. P., Stevens, A. R. H., Bower, R. G., et al. 2018, MNRAS, 473, 4956
Lange, R., Driver, S. P., Robotham, A. S. G., et al. 2015, MNRAS, 447, 2603
Leaman, R., Venn, K. A., Brooks, A. M., et al. 2012, ApJ, 750, 33
Lelli, F., McGaugh, S. S., & Schombert, J. M. 2016a, AJ, 152, 157
Lelli, F., McGaugh, S. S., & Schombert, J. M. 2016b, ApJ, 816, L14
Leroy, A. K., Walter, F., Brinks, E., et al. 2008, AJ, 136, 2782
Lutz, K. A., Kilborn, V. A., Koribalski, B. S., et al. 2018, MNRAS, 476, 3744
Macciò, A. V., Dutton, A. A., & van den Bosch, F. C. 2008, MNRAS, 391, 1940
Mancera Piña, P. E., Fraternali, F., Oman, K. A., et al. 2020, MNRAS, 495, 3636
Marasco, A., Fraternali, F., Posti, L., et al. 2019, A&A, 621, L6
Marshall, M. A., Mutch, S. J., Qin, Y., Poole, G. B., & Wyithe, J. S. B. 2019, MNRAS, 488, 1941
Martinsson, T. P. K., Verheijen, M. A. W., Westfall, K. B., et al. 2013, A&A, 557, A130
Martinsson, T. P. K., Verheijen, M. A. W., Bershady, M. A., et al. 2016, A&A, 585, A99
Mo, H. J., Mao, S., & White, S. D. M. 1998, MNRAS, 295, 319
Murugeshan, C., Kilborn, V., Obreschkow, D., et al. 2019, MNRAS, 483, 2398
Murugeshan, C., Kilborn, V., Jarrett, T., et al. 2020, MNRAS, 496, 2516
Navarro, J. F., & Steinmetz, M. 2000, ApJ, 538, 477
Newville, M., Stensitzki, T., Allen, D. B., & Ingargiola, A. 2014, `https://doi.org/10.5281/zenodo.11813`
Noordermeer, E. 2006, PhD Thesis, Kapteyn Astronomical Institute, University of Groningen, The Netherlands
Noordermeer, E., Merrifield, M. R., & Aragón-Salamanca, A. 2008, MNRAS, 388, 1381
Obreja, A., Stinson, G. S., Dutton, A. A., et al. 2016, MNRAS, 459, 467
Obreschkow, D., & Glazebrook, K. 2014, ApJ, 784, 26
Obreschkow, D., Glazebrook, K., Kilborn, V., & Lutz, K. 2016, ApJ, 824, L26
Oliphant, T. E. 2007, Comput. Sci. Eng., 9, 10
Ott, J., Stilp, A. M., Warren, S. R., et al. 2012, AJ, 144, 123
Pedrosa, S. E., & Tissera, P. B. 2015, A&A, 584, A43
Peebles, P. J. E. 1969, ApJ, 155, 393
Pezzulli, G., Fraternali, F., & Binney, J. 2017, MNRAS, 467, 311
Ponomareva, A. A., Verheijen, M. A. W., & Bosma, A. 2016, MNRAS, 463, 4052
Ponomareva, A. A., Verheijen, M. A. W., Peletier, R. F., & Bosma, A. 2017, MNRAS, 469, 2387
Posti, L., Fraternali, F., Di Teodoro, E. M., & Pezzulli, G. 2018a, A&A, 612, L6
Posti, L., Pezzulli, G., Fraternali, F., & Di Teodoro, E. M. 2018b, MNRAS, 475, 232
Posti, L., Marasco, A., Fraternali, F., & Famaey, B. 2019a, A&A, 629, A59
Posti, L., Fraternali, F., & Marasco, A. 2019b, A&A, 626, A56
Read, J. I., Iorio, G., Agertz, O., & Fraternali, F. 2016, MNRAS, 462, 3628
Read, J. I., Iorio, G., Agertz, O., & Fraternali, F. 2017, MNRAS, 467, 2019
Romanowsky, A. J., & Fall, S. M. 2012, ApJS, 203, 17
Romeo, A. B. 2020, MNRAS, 491, 4843
Sancisi, R., Fraternali, F., Oosterloo, T., & van der Hulst, T. 2008, A&ARv, 15, 189
Sanders, R. H. 1996, ApJ, 473, 117
Sanders, R. H., & Verheijen, M. A. W. 1998, ApJ, 503, 97
Somerville, R. S., Behroozi, P., Pandya, V., et al. 2018, MNRAS, 473, 2714
Steinmetz, M., & Navarro, J. F. 1999, ApJ, 513, 555
Stevens, A. R. H., Croton, D. J., & Mutch, S. J. 2016, MNRAS, 461, 859
Stevens, A. R. H., Lagos, C. D. P., Obreschkow, D., & Sinha, M. 2018, MNRAS, 481, 5543
Swaters, R. A. 1999, PhD Thesis, Kapteyn Astronomical Institute, University of Groningen, The Netherlands
Swaters, R. A., van Albada, T. S., van der Hulst, J. M., & Sancisi, R. 2002, A&A, 390, 829
Swaters, R. A., Sancisi, R., van Albada, T. S., & van der Hulst, J. M. 2009, A&A, 493, 871
Sweet, S. M., Fisher, D. B., Savorgnan, G., et al. 2019, MNRAS, 485, 5700
Sweet, S. M., Glazebrook, K., Obreschkow, D., et al. 2020, MNRAS, 494, 5421
Tully, R. B., Courtois, H. M., Dolphin, A. E., et al. 2013, AJ, 146, 86
van den Bosch, F. C., Burkert, A., & Swaters, R. A. 2001, MNRAS, 326, 1205
van der Hulst, J. M., van Albada, T. S., & Sancisi, R. 2001, in Gas and Galaxy Evolution, eds. J. E. Hibbard, M. Rupen, & J. H. van Gorkom, ASP Conf. Ser., 240, 451
van der Kruit, P. C. 1988, A&A, 192, 117
van der Kruit, P. C., & Searle, L. 1981, A&A, 95, 105
van der Marel, R. P., Alves, D. R., Hardy, E., & Suntzeff, N. B. 2002, AJ, 124, 2639
Verheijen, M. A. W., & Sancisi, R. 2001, A&A, 370, 765
Virtanen, P., Gommers, R., Oliphant, T. E., et al. 2020, Nat. Meth., 17, 261
Wechsler, R. H., & Tinker, J. L. 2018, ARA&A, 56, 435
Wen, X.-Q., Wu, H., Zhu, Y.-N., et al. 2013, MNRAS, 433, 2946
Young, T., Jerjen, H., López-Sánchez, Á. R., & Koribalski, B. S. 2014, MNRAS, 444, 3052
Zanisi, L., Shankar, F., Lapi, A., et al. 2020, MNRAS, 492, 1671
Zhang, H.-X., Hunter, D. A., Elmegreen, B. G., Gao, Y., & Schruba, A. 2012, AJ, 143, 47
Zoldan, A., De Lucia, G., Xie, L., Fontanot, F., & Hirschmann, M. 2018, MNRAS, 481, 1376

Appendix A: Kinematic modelling of LVHIS, WHISP, and VLA-ANGST dwarfs

The Local Volume H I Survey (LVHIS, Koribalski et al. 2018), the Westerbork observations of neutral Hydrogen in Irregular and SPiral galaxies (WHISP, van der Hulst et al. 2001) and the Very Large Array-ACS Nearby Galaxy Survey Treasury (VLA-ANGST, Ott et al. 2012) projects, provide deep interferometric observations of a large set of gas–rich nearby galaxies. Full details on the characteristic of the surveys, including targets, observations and data reduction procedures can be found in the references above.

Given that highly reliable rotation curves are needed to estimate the specific angular momentum, we selected the dwarf galaxies in LVHIS, WHISP, and VLA-ANGST that were the most suitable to perform kinematic modelling on them (and in the case of WHISP, galaxies that are not already modelled by Swaters et al. 2002 and included in SPARC). We chose the best galaxies in terms of spatial resolution (at least five resolution elements) and undisturbed gas kinematics (galaxies without interacting neighbours or strong non-circular motions). We are mainly interested in dwarf galaxies with moderate rotation velocities, so we kept those galaxies with an observed velocity field suggesting rotation velocities below ~80 km s^{-1}.

We analyzed the galaxies using the software $^{\rm 3D}$BAROLO (Di Teodoro & Fraternali 2015), fitting the rotation velocity, velocity dispersion, inclination, and position angle. Initial estimates on inclination and position angle are determined by fitting the observed H I map, following the procedure described in Mancera Piña et al. (2020). All the models converged with very good resemblance to the data. Importantly, we corrected the rotational speed $V_{\rm rot}$ for pressure-supported motions in the gas –often non-negligible in dwarf galaxies (e.g., Iorio et al. 2017). This is crucial as the circular speed ($V_{\rm c}^2 = V_{\rm rot}^2 + V_{\rm AD,gas}^2$) is needed to obtain the stellar rotation curve ($V_*^2 = V_{\rm c}^2 - V_{\rm AD,*}^2$), as described in Sect. 3.

After rejecting galaxies with inclinations below 30° (for which small uncertainties in inclination translate into big uncertainties in the deprojected rotation velocity) and above 75° (for which tilted-ring models are not well suited due to the overlapping of different line-of-sights), we ended up with 14 galaxies from LVHIS (LVHIS 9, 12, 20, 25, 26, 29, 30, 55, 60, 65, 72, 74, 78, and 80), four from VLA-ANGST (DDO 181, DDO 183, DDO 190, and NGC 4190) and three from WHISP (UGC 9649, UGC 10564, and UGC 12060). The galaxies have redshift-independent distance determinations from Karachentsev et al. (2007), Dalcanton et al. (2009), Tully et al. (2013), and Bouquin et al. (2018), coming mostly from the tip of the red giant branch.

For those galaxies with kinematic parameters in the literature (e.g., Kirby et al. 2012; Kamphuis et al. 2015), the recovered projected rotation velocities are usually in good agreement with the values obtained with $^{\rm 3D}$BAROLO, but the shape of our rotation curves are generally smoother. Figure A.1 shows five representative galaxies fitted with $^{\rm 3D}$BAROLO: velocity field (observed and modelled), position-velocity diagram along the major axis (observed and modelled), and the recovered rotation curve before and after correcting for asymmetric drift, as well as the velocity dispersion profile. The ring-by-ring parameters (rotation velocity, velocity dispersion, circular speed, and gas surface density) of the 21 galaxies as obtained from $^{\rm 3D}$BAROLO are available upon request.

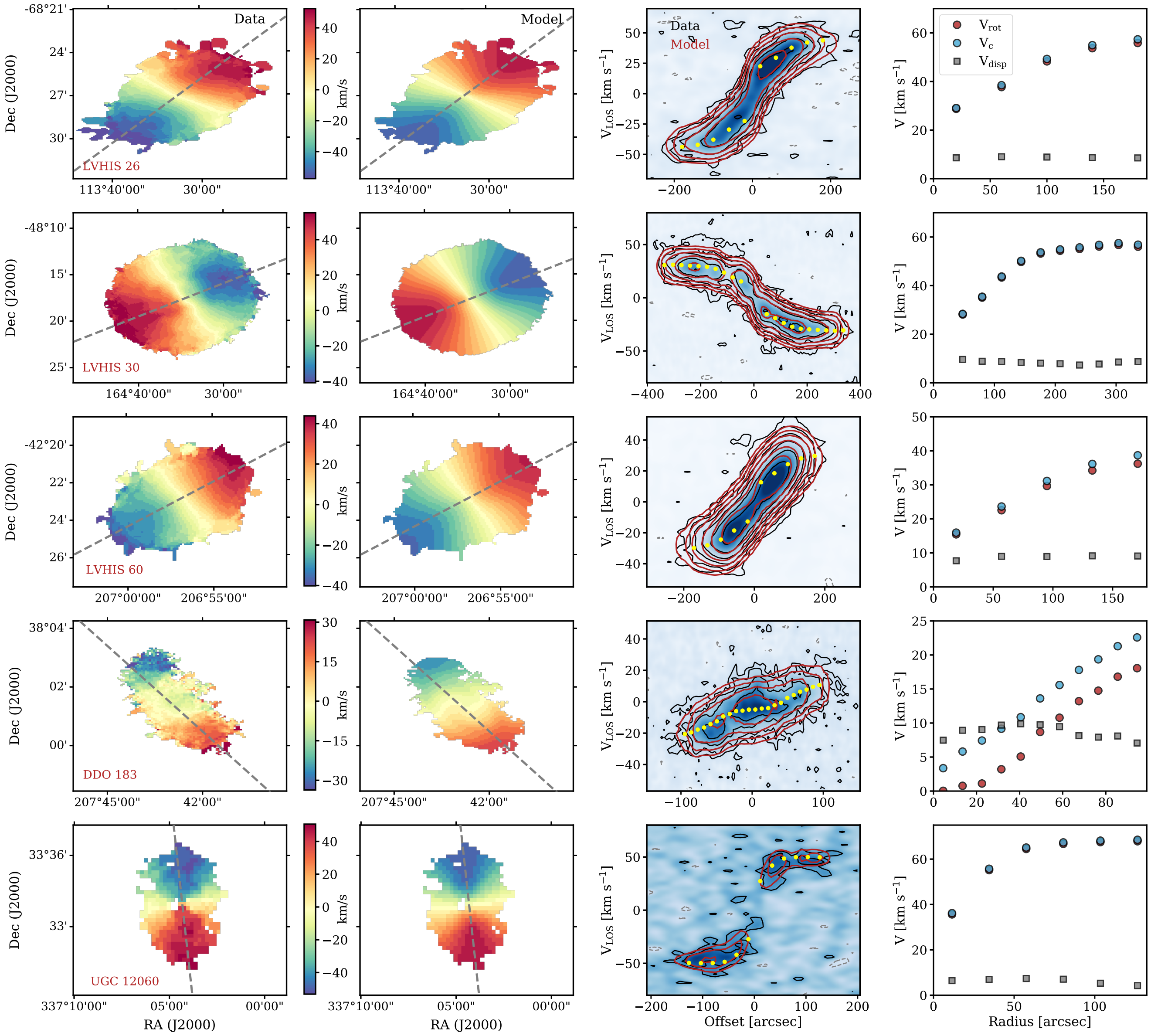

Fig. A.1. Kinematic models of five representative galaxies obtained with $^{3\rm D}$BAROLO. *From left to right*: (1) observed and (2) best-fitting model velocity field; the dashed grey line shows the average kinematic position angle, while the bar between the two panels show the colour scheme in both velocity fields. (3) Major axis position-velocity diagram: The data is shown in blue, while black contours enclose the data (grey for negative values) and red contours the best-fitting model. The contour levels are at −2, 2, 4, 8, 16, . . . times the mean rms in the corresponding data cube. The recovered rotation velocities are shown in yellow. (4) Rotation velocity (red), circular speed (blue) and velocity dispersion (grey) profiles.

Appendix B: Robustness of *j*–*M* relations

B.1. Robustness against stellar-asymmetric drift correction

Since we made a series of assumptions while deriving $V_{\mathrm{AD}*}$ (and thus j_* and j_{bar}), it is important to understand how do changes in these assumptions affect the results shown in this work. We do not expect these assumptions to play a significant role in our determination of j_{bar}: At high M_{bar}, j_{bar} is dominated by the stellar component, but in that regime the asymmetric drift correction is often negligible (see for instance Fig. 3); at low M_{bar} the correction becomes more important, but then j_{bar} is dominated by the gas component, which is unaffected by $V_{\mathrm{AD}*}$. Therefore, the $j_{\mathrm{bar}}-M_{\mathrm{bar}}$ relation is robust against different ways of determining $V_{\mathrm{AD}*}$. Yet, the correction may play a role at the low j_*-regime of the j_*-M_* relation, even if it not as strong as expected from the stellar rotation curve: $V_{\mathrm{AD}*}$ affects V_* more strongly at large radii, but j_* is also proportional to Σ_* (see Eq. (1)), which decreases with radius. In the next paragraphs we investigate how these two facts affect j_*.

As mentioned before, our calculation of $V_{\mathrm{AD}*}$ is empirically motivated, and we used a floor value of $10\,\mathrm{km\,s^{-1}}$ for the stellar velocity dispersion $\sigma_{*,z}$. To test how much our measurements of j_* and j_{bar} would change by following different prescriptions, we perform two tests where we investigate two extreme scenarios. In the first scenario co-rotation of gas and stars is assumed, and this is we maximize j_* and j_{bar} by setting $V_{\mathrm{AD}*} = 0$. In the second scenario, we minimize j_* and j_{bar} by adopting a floor value for $\sigma_{*,z}$ of $15\,\mathrm{km\,s^{-1}}$. This floor is clearly too high given the observed values of $\sigma_{*,z}$ in the outskirts of galaxies (e.g., Swaters 1999; Martinsson et al. 2013), but it is still interesting as an extreme case.

The result is shown in Fig. B.1, where we compare our fiducial best-fitting stellar (left) and baryonic (right) *j*–*M* laws (grey bands), as obtained in Sect. 4, with the values obtained from the two scenarios mentioned above: no asymmetric drift correction (top) and extreme asymmetric drift correction (bottom). We note that, as in Fig. 5, the galaxies in the left panels are not necessarily the same as in right panels.

We start by looking and the j_*-M_* relation, shown in the left panels of Fig. B.1. Both cases are still reasonably well fitted by the fiducial model, both in terms of slope and intercept and in terms of its intrinsic orthogonal scatter. The extreme scenario slightly reduces j_* for most of the galaxies, but it also makes a number (27) of them end up with unreliable j_* (and j_{bar}) because their stellar rotation curves have extremely large uncertainties and some are even compatible with zero. Because of this, 14 galaxies (the 14 with convergent profiles of the 27 affected galaxies, mostly dwarfs) were removed from the figure. Leaving aside this drawback, the main j_*-M_* for the remaining galaxies is not strongly affected. A final caveat about this is that there are very few dwarf galaxies with both stellar and H I rotation curves, so testing how accurate is the determination of the asymmetric drift correction (by comparing the stellar and neutral gas rotation curve) remains an open issue.

The right hand side panels of Fig. B.1 show the $j_{\mathrm{bar}}-M_{\mathrm{bar}}$ laws considering the different j_* from the left hand side. It is clear that the baryonic relation is very robust against the asymmetric drift correction, as expected from our reasoning above. The points derived under both stellar asymmetric drift regimes are always well described by our fiducial best-fitting model. Fitting the points with Eq. (7) gives coefficients $\alpha = 0.59 \pm 0.02$, $\beta = 2.80 \pm 0.03$, and $\sigma_\perp = 0.18 \pm 0.02$ for the case of co-rotation of gas and stars, and $\alpha = 0.58 \pm 0.03$, $\beta = 2.81 \pm 0.03$, and $\sigma_\perp = 0.14 \pm 0.02$ for the strong $V_{\mathrm{AD}*}$. We can see then that even under extreme assumptions the $j_{\mathrm{bar}}-M_{\mathrm{bar}}$ relation is robust against the way of determining the asymmetric drift correction.

As discussed before, the small differences were certainly expected for the $j_{\mathrm{bar}}-M_{\mathrm{bar}}$ relation, but not necessarily for the stellar component. To further investigate this, we compare the corrected (fiducial case) and non-corrected ($V_{\mathrm{AD}*} = 0$) values of j_* as a function of M_* for all the galaxies in our sample, as shown in Fig. B.2. It becomes even clearer that the correction affects more low-M_* galaxies, as shown both by the observational points and by the running mean of the distribution (dashed blue line).

The median ratio between corrected and non-corrected j_* is 0.96. If we look at galaxies with $M_* < 10^9\,M_\odot$ this ratio drops by $\sim$5%. Figure B.2 demonstrates that while the asymmetric drift correction does not strongly affect the j_* for the bulk of our galaxy sample, it is still important to correct on an individual basis because, for some of our dwarfs, the correction can account for a decrease in j_* of up to 40%.

B.2. Robustness against convergence criterion $\mathcal{R}$

We use the convergence criterion $\mathcal{R} \geq 0.8$ to select our final sample of galaxies (see Sect. 3.2). Based on tests using galaxies with clearly converging profiles we find that $\mathcal{R} \geq 0.8$ allows for sub-0.1 dex recoveries of *j*. In this appendix we explore how different assumptions on $\mathcal{R}$ affect the final shape of the $j_{\mathrm{bar}}-M_{\mathrm{bar}}$ relation. In particular, we explore the stricter case where $\mathcal{R} \geq 0.9$, and the extreme case of $\mathcal{R} > 0$ (and this is not applying any convergence criterion for our sample). Figure B.3 presents the $j_{\mathrm{bar}}-M_{\mathrm{bar}}$ law under these test assumptions: The left and right panel show the relation for $\mathcal{R} \geq 0.9$ and $\mathcal{R} > 0$, respectively.

In the case of $\mathcal{R} \geq 0.9$, by fitting the points with Eq. (7) we find the best-fitting parameters (not shown in Fig. B.3) $\alpha = 0.56 \pm 0.03$, $\beta = 2.74 \pm 0.03$, and $\sigma_\perp = 0.12 \pm 0.02$, very similar to the values found for $\mathcal{R} \geq 0.8$ (Table 2). The sample is reduced, especially at M_{bar} below $10^{9.5}\,M_\odot$, which contributes to a marginal decrease (but still consistent within uncertainties) in the slope of the relation.

For the case where no convergence criterion is applied we find $\alpha = 0.61 \pm 0.02$, $\beta = 2.83 \pm 0.03$, and $\sigma_\perp = 0.14 \pm 0.01$ (not shown in Fig. B.3). The slope is slightly steeper than for the cases $\mathcal{R} \geq 0.8$ and $\mathcal{R} \geq 0.9$, but consistent within uncertainties. The intercept is also slightly higher, and the intrinsic scatter remains basically the same. We can see, however, that while the best-fitting parameters are not significantly affected by the convergence criterion as the bulk of the sample is not affected (likely related with the large extent of our rotation curves and surface density profiles), there are a number of galaxies with lower j_{bar} than the average, as expected from removing the convergence criterion.

B.3. Robustness against the stellar mass-to-light ratio

It is well known that using near-infrared surface brightness profiles, as we do in this work, is important to accurately trace the mass distributions of galaxies (e.g., Verheijen & Sancisi 2001; Lelli et al. 2016b). While j_* and j_{gas} do not depend on Υ, j_{bar}, and M_{bar} do, since they depend on f_{gas}. In this section we address how changes in Υ affect the $j_{\mathrm{bar}}-M_{\mathrm{bar}}$ relation. We note that our uncertainties in M_* (and thus our uncertainties in f_{gas}, M_{bar}, and j_{bar}) always include an uncertainty term coming from Υ: $\sigma_\Upsilon = 0.11$ dex for the 3.6 μm profiles (Lelli et al. 2016b) and

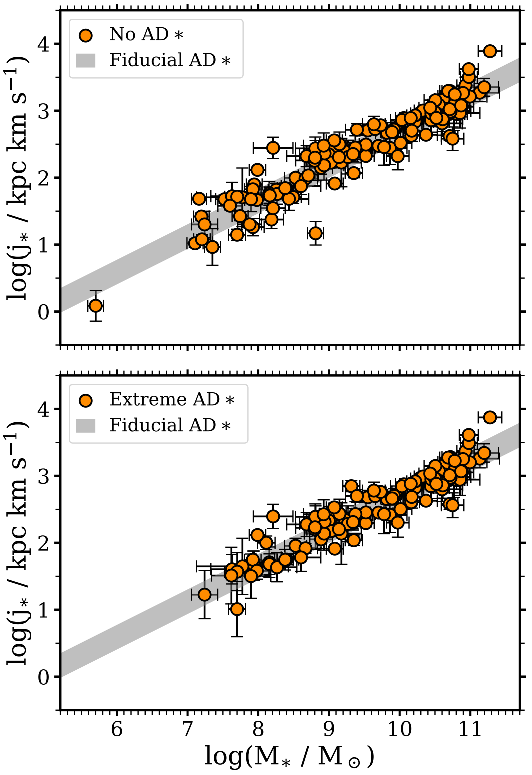

Fig. B.1. Stellar (*left*) and baryonic (*right*) j–M relations under the assumption of none (*top*) or extreme (*bottom*) asymmetric drift correction. In all the panels, the grey band corresponds to the best-fitting relation found for our fiducial correction (see Table 2). Since we applied a convergence criterion, the galaxies are not exactly the same in all the panels.

$\sigma_\Upsilon = 0.3$ dex for the *H*-band profiles (Kirby et al. 2008; Young et al. 2014).

We performed two tests, building again the baryonic j–M plane, but lowering and raising Υ by 1σ but keeping our convergence criterion of $\mathcal{R} \geq 0.8$. The results are shown in Fig. B.4, where we compare the new sets of points with our fiducial best-fitting $j_{\rm bar}$–$M_{\rm bar}$ law (grey band, see Sect. 4). Naturally, the low-Υ generates a small shift towards lower masses with respect to the fiducial relation, while the high-Υ shifts galaxies rightwards. Fitting the low- and high-Υ $j_{\rm bar}$–$M_{\rm bar}$ relations gives best fitting parameters (α, β, $\sigma_\perp$) of (0.61, 2.82, 0.14) and (0.58, 2.75, 0.16), respectively. The fiducial Υ gives intermediate best-fitting parameters with respect to these two cases. Importantly, the slopes are compatible within their uncertainties, so we can conclude that the baryonic j–M law is robust against the exact choice of the stellar mass-to-light ratio.

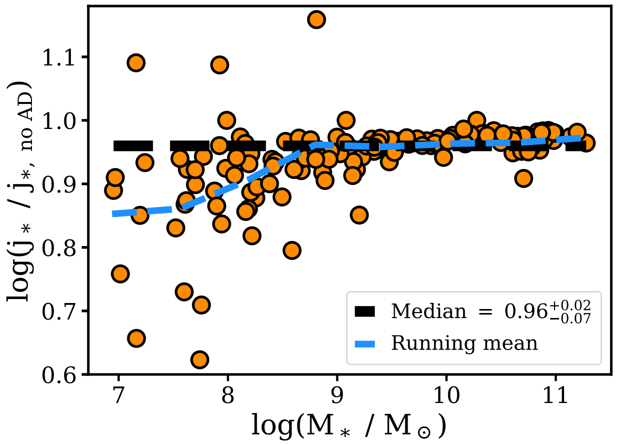

Fig. B.2. Ratio between values of the stellar specific angular moment obtained when the asymmetric drift correction is applied (j_*) or not ($j_{*,\rm no\,AD}$), i.e. co-rotation if stars and gas is assumed, as a function of M_*. Orange points show the ratios for each galaxy, while the dashed black and blue lines show the median of the distribution and the running mean, respectively. Three galaxies have a larger j_* when the asymmetric drift correction is applied. This is because those galaxies have a strong contribution of pressure-supported motions, such that the stellar rotation curve derived from the circular speed profile has a larger amplitude than the H I rotation curve.

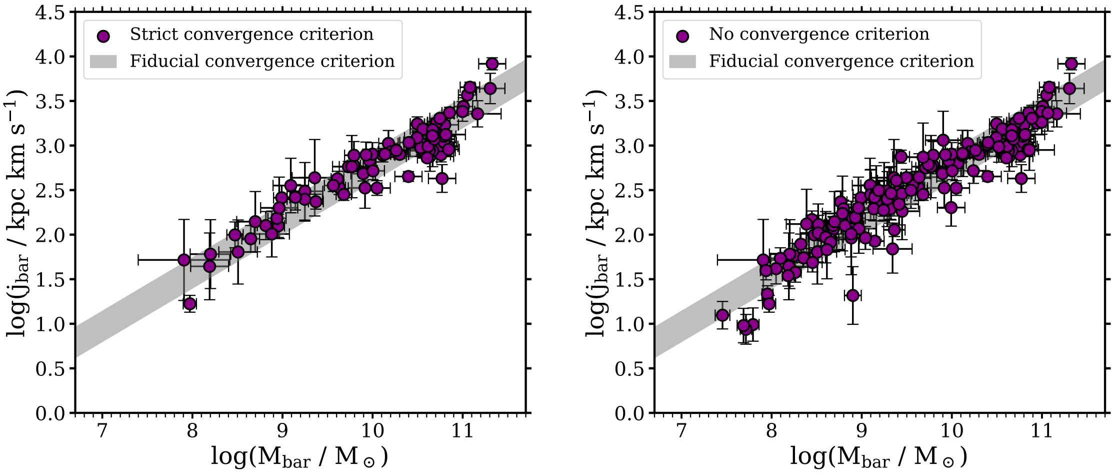

Fig. B.3. $j_{\rm bar}$–$M_{\rm bar}$ law under different assumptions for the convergence criterion. *Left panel*: galaxies that meet $\mathcal{R} \geq 0.9$, *right panel*: case where no criterion convergence is applied ($\mathcal{R} > 0$). In both panels, the grey band shows the best-fitting power-law found in Sect. 4 for the fiducial convergence criterion $\mathcal{R} \geq 0.8$.

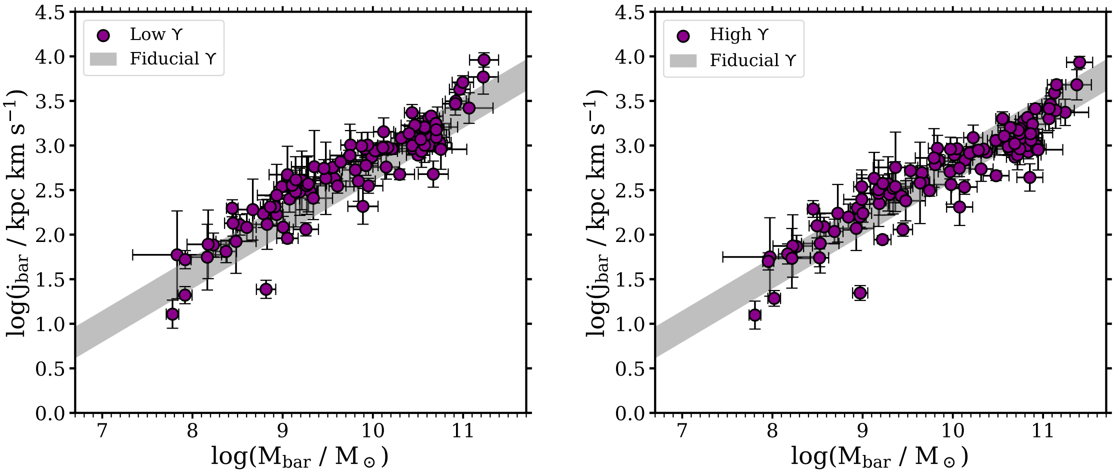

Fig. B.4. $j_{\rm bar}$–$M_{\rm bar}$ law under different assumptions for the mass-to-light ratio Υ for the convergence criterion. *Left* and *right panels*: data points obtained by lowering and increasing our fiducial Υ by 1σ, respectively. In both panels, the grey band shows the best-fitting power-law found in Sect. 4 for the fiducial Υ.